Macroscopic softening in granular materials from a mesoscale perspective

Jiaying Liu, Antoine Wautier, Stéphane Bonelli, François Nicot, Félix Darve

Macroscopic softening in granular materials from a mesoscale perspective

Jiaying Liu, Antoine Wautier, Stéphane Bonelli, François Nicot, Félix Darve

Macroscopic softening in granular materials from a mesoscale perspective

Jiaying LIU[a,c], Antoine WAUTIER[b,c,*], Stéphane BONELLI[b], François NICOT[c], Félix DARVE[d]

[a] *State Key Laboratory of Water Resources and Hydropower Engineering Science, Wuhan University, Wuhan 430072, China*

[b] *INRAE, Aix-Marseille University, UR RECOVER, 3275 Rte Cézanne, CS 40061, 13182 Aix-en-Provence Cedex 5, France.*

[c] *Université Grenoble Alpes, INRAE, UR ETGR, 2 rue de la Papeterie-BP 76, F-38402 St-Martin-d'Hères, France.*

[d] *Université Grenoble Alpes, CNRS, G-INP, Laboratoire 3SR UMR5521, F-38000 Grenoble, France*

Abstract

Stress-oftening is one of the significant features experienced by cohesive-frictional granular materials subjected to deviatoric loading. This paper focuses on mesoscopic evolutions of the dense granular assembly during a typical drained biaxial test conducted by DEM, and proposes mesoscopically-based framework to interpret both hardening and softening mechanisms. In this context, force chains play a fundamental role as they form the strong contact phase in granular materials. Their geometrical and mechanical characteristics, as well as the surrounding structures, are defined and analyzed in terms of force chain bending evolution, local dilatancy, rotation and non coaxiality between the principal stress and the geometrical orientation of force chains. By distinguishing two zones inside and outside shear band, force chain rotations are shown to be of opposite sign, which may contribute to the observed macroscopic softening as one of the origin of the structural softening.

Keywords: DEM, granular materials, softening, mesomechanics, force chains, strain localization, rotation

---

1. Introduction

When going down to the microscale granular materials may appear deceptively simple but at the macroscale, the huge number of internal degrees of freedom results in very complex behaviors (Suiker et al., 2001; Roux, 2000; Kruyt, 2010; Tordesillas et al., 2016). It is widely accepted that the macroscopic mechanical responses are due to the combination of local contact mechanics and the geometrical arrangement of the granular assembly. Strain softening is maybe one of the most

*Corresponding author
Email address: `antoine.wautier@inrae.fr` (Antoine WAUTIER)

puzzling features in cohesive-frictional granular media. Opposite to strain hardening, strain softening corresponds in plasticity theory to negative values for the hardening modulus. Being able to capture accurately this feature has been one of the key issues in constitutive modeling of geomaterials for decades. Two kinds of softening can be distinguished depending on the loading conditions (Sterpi, 1999): the "material softening" which is an intrinsic material property and the "structural softening" for which the decrease in the shear resistance is related to the loss of homogeneity due to strain localization. Drained triaxial tests are often used to characterize strain softening experimentally. Contrary to the undrained triaxial test stress reduction observed during this test is partly driven by the boundary conditions. If no loss of homogeneity is observed, the experimental test directly characterizes the material softening as a consequence of the change in the plastic behaviors from strain hardening to strain softening. Otherwise, the test characterizes a structural softening as the sample is composed of two zones: the shear band domain where the material experiences locally material softening (Zhu et al., 2016a) and the rest of the sample where the plasticity is hardly not activated. The mathematic descriptions of the classical stress-strain relationship including softening phase have been mentioned in many constitutive models (Lade, 1977; Sterpi, 1999), and typically for non-cohesive granular soils, state-dependent models have been suggested (Been and Jefferies, 1985; Wan and Guo, 1998; Li and Dafalias, 2000; Sun et al., 2017). However, we do mention that while structural softening takes place within a given material specimen, the notion of constitutive behavior disappears on that specimen scale.

Recently, perspectives at the micro- and mesoscale have been opened with the introduction of efficient simulation tools (e.g. DEM, Discrete Element Method) and laboratory imaging techniques (e.g., X-Ray Computed Tomography, Digital Image Correlation and Photoelastic stress analysis). The micro- and mesoscale information can help understand the underlying mechanisms behind macroscopic observations and incorporate more physics in constitutive modeling. The microscopic scale investigations focus on individual particle kinematics and contact dynamics, in some cases particle breakage is considered (Ma et al., 2014, 2017; Yin et al., 2016; Zhou et al., 2015); while at the mesoscopic scale, structural features are accounted for with clusters of a few particles such as force chains and grain loops (in 2D) (Tordesillas et al., 2010; Zhu et al., 2016b). These two types of mesostructures can stand as the dual characteristics of granular contact systems (Radjai et al., 1996, 1998). Mesoscopic investigations have succeeded in explaining significant mechanisms in granular materials, such as failure modes (e.g., Zhu et al. (2016a)), instability (e.g., Rechenmacher et al. (2011); Wautier et al. (2018)) and shear band forming (e.g.,Tordesillas (2007)). As a result, mesostructure-based constitutive models have been proposed as a convenient way to homogenize the mechanical behavior of granular materials (Nicot and Darve, 2011; Xiong et al., 2017).

The manuscript attempts to show the extent to which mesoscale analysis can address the macroscopic softening in granular materials. In previous contributions (Tordesillas and Muthuswamy, 2009; Zhu et al., 2016a), the force chain bending was focused on, which was regarded as the local failure of the mesostructure (Tordesillas and Muthuswamy, 2009; Nicot et al., 2017). Walker and Tordesillas (2010); Zhu et al. (2016b) claimed that the development of force chain bending is related to the characteristic point (the switch between contractive and dilative behaviors before the stress peak) of a biaxial test for dense granular assembly. At the same time, the fraction of sliding contacts decreases and contact sliding localizes within some subdomains (Liu et al., 2018), and a non-affine deformation mode is identified (Ma et al., 2018).

Internal structures become unstable before the macroscopic limit state is reached. It is therefore necessary to describe and define the softening at the mesoscale as an indication of prefailure mechanism for the bulk. To this respect, the mechanical and geometrical evolutions of mesostructures should be significant to the softening occurence in granular materials, and interactions between force chains and 2D loops mentioned by Zhu et al. (2016b); Tordesillas et al. (2010), is somehow thought to influence the hardening/softening transition.

In this paper, the structural softening accompanied by shear banding is emphasized by mainly focusing on dense granular materials subjected to drained tests. Investigations at the micro- and meso-levels were carried out, and the hardening and softening phase mechanisms are explored in terms of mesoscopic stress, strain and fabric evolutions. In particular, we analyze how the force chains and the surrounding loops control the mechanical responses at the mesoscopic scale. It should be noted that when softening occurs and one shear band forms, mesoscopic characteristics are investigated separately inside and outside shear band.

This paper is organized as follows. In Section 2 two numerical samples are prepared and subjected to drained biaxial tests. Thanks to the use of grain loop and force chain analysis, the respective micro to macro links between grain displacements and strain, and also between contact forces and stress are reviewed and discussed. Section 3 provides a comprehensive study on the mesoscopic stress, fabric and topology exchanges, which are consistent with macroscopic stress-strain responses. Finally, Section 4 focuses on the strain softening induced by the structural change (shear band). The rotations of force chain fabric and principal stresses are found, and the failure mechanism of force chains is discussed.

2. Biaxial test and granular mesostructures

In this section, the basic macroscopic stress-strain relationships of biaxial tests are recalled for grain assemblies with two densities. Mesostructure definitions are introduced and a particular care is paid to locally define the strain and stress indicators able to account for macroscopic observations. Contrary to other coarse graining approaches, the use of mesostructures is central in our approach to bridge the gap between micro and macro scales.

2.1. Numerical set up and macroscopic responses

Biaxial tests are carried out numerically with the use of the open-source DEM software YADE (Šmilauer et al., 2015). The granular assemblies are generated within a rectangular box of aspect ratio 1.5 (shown in Figure 1), containing a single layer of 20,000 spheres with a uniform distribution of diameters ($d_{50} = 0.008$ m and $d_{\max}/d_{\min} = 2$). Dense and loose specimens are compressed to an isotropic desired confining state of 4 kN/m, with initial parameters listed in Table 1. During the preparation of dense and loose samples, different friction angles ϕ (2° for the dense and 35° for the loose) are set to reach a large density gap between them. When biaxial conditions are met under loading process, ϕ is set to 35° for both the samples. In Table 1, n is the 2D porosity of the assembly, Z_m is the initial coordination number, k_n and k_t are the normal and tangential stiffness of the contact model, $d_s = 2R_1R_2/(R_1+R_2)$ is the harmonic average of the raddii of the particles in contact and ϕ is the contact friction angle between spheres. To accelerate the simulations, the numerical damping coefficient is set to 0.25 (see details in Šmilauer et al. (2015) for its definition).

Table 1: Initial isotropic states and loading parameters of dense and loose specimen.

Specimen	n	Z_m	k_n/d_s	k_t/k_n	ϕ
Dense	0.161	4.01	300 MPa	0.5	35°
Loose	0.207	3.06	300 MPa	0.5	35°

Typical macro stress-strain relations are shown in Figure 2. For the dense sample, the deviatoric stress ($q = \sigma_1 - \sigma_2$ where σ_1 and σ_2 are the major and minor principal stresses) demonstrates a peak for $\varepsilon_{22} = 0.014$. Before this point, the stress state of the assembly is in the hardening regime while after that the sample stress state is in the softening regime[1]. The volumetric strain evolution of the

[1] As recalled in the introduction, the distinction between the hardening and softening regimes can be read directly on the stress strain curve for drained biaxial test.

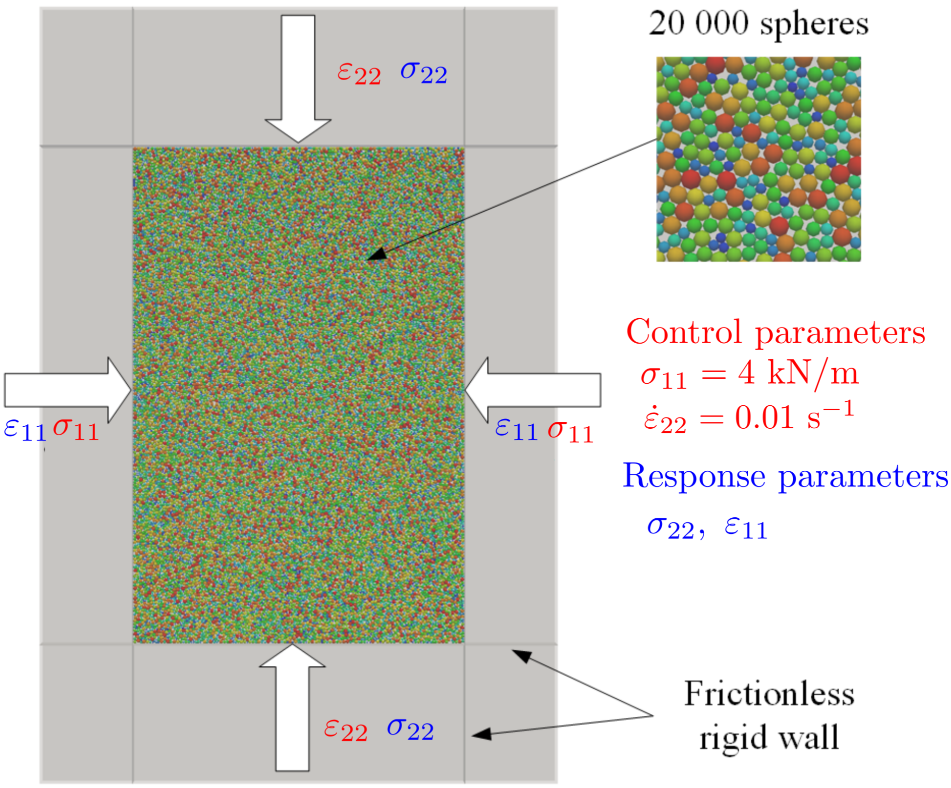

Figure 1: DEM specimen for biaxial tests.

dense sample also shows a characteristic point around $\varepsilon_{22} = 0.01$, which corresponds to the transition from contractancy to dilatancy (characteristic point). As a result, 3 stages can be identified in Figure 2(a):

- Stage I — hardening phase with shear contractancy;
- Stage II — hardening phase with shear dilatancy;
- Stage III — softening phase with shear dilatancy.

For the loose specimen, neither softening nor dilative characteristics are observed.

2.2. *Contact based loop and local strain definition*

For 2D granular materials, the contact network can be used to provide a partition of the material domain into polygonal shapes forming grain loops (Kuhn, 1999; Kruyt and Rothenburg, 1996; Satake, 1992). The loops play an important role in volumetric and anisotropic evolutions, as they contain deformable pores. An example of the 2D loop tessellation is given in Figure 3. The larger the loop valence (the number of particles within the given loop), the larger its deformability. A number of

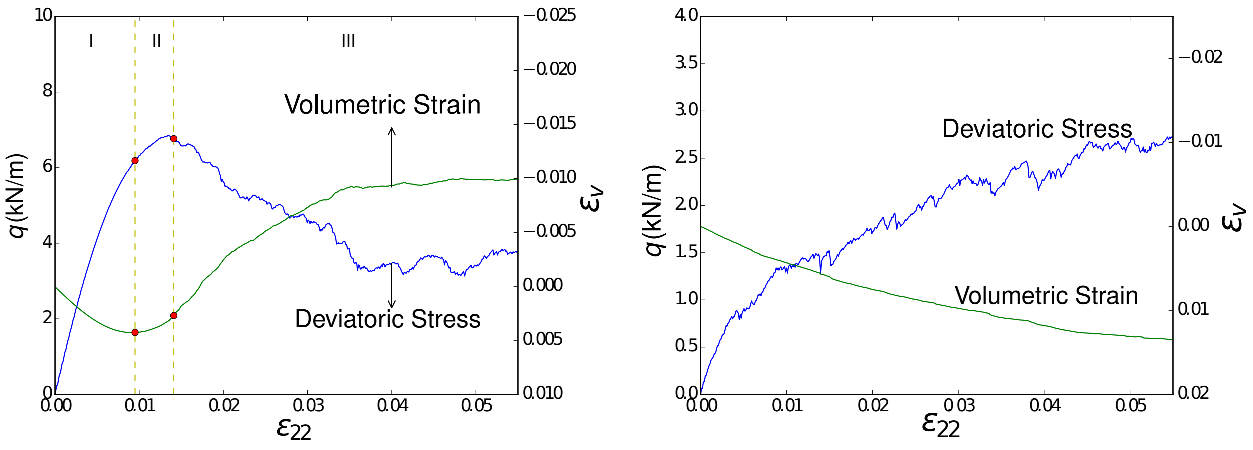

(a) Dense sample (b) Loose sample

Figure 2: Macro stress strain relations during the biaxial loading for the dense (a) and loose (b) specimens.

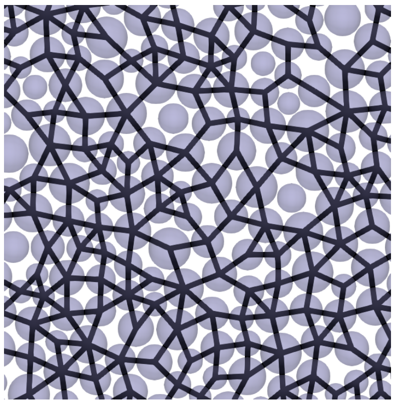

Figure 3: An example of 2D loop tessellation in granular materials

studies were conducted to describe the topological compositions (Zhu et al., 2016a,b; Tordesillas et al., 2010) and mechanical characteristics (Kuhn, 1999; Nguyen et al., 2012) of 2D loops.

Under certain assumptions, strain definitions based on these local loops can been proposed (Kuhn, 1999; Bagi, 1996; Li and Yu, 2009; Dedecker et al., 2000; Wang et al., 2007; Cambou et al., 2013). In this paper, a simple 2D definition is adopted by assuming uniform deformation within each loop L:

$$\varepsilon_{ij} = \frac{1}{|L|} \int_L \frac{u_{i,j} + u_{j,i}}{2} \mathrm{d}S \tag{1}$$

where $|L|$ is the area of the loop domain L and $u_{i,j} = \frac{\partial u_i}{\partial x_j}$ is the gradient of displacement field within L. The definition of 3D loops is however a difficult task because of void connectivity and the notion of loop has to be replaced by grain clusters (containing grains and internal pores) for instance.

For an enclosed system, the integration can be changed to the loop boundary ∂L:

$$\varepsilon_{ij} = \frac{1}{|L|} \int_{\partial L} \frac{u_i n_j + u_j n_i}{2} \mathrm{d}l \tag{2}$$

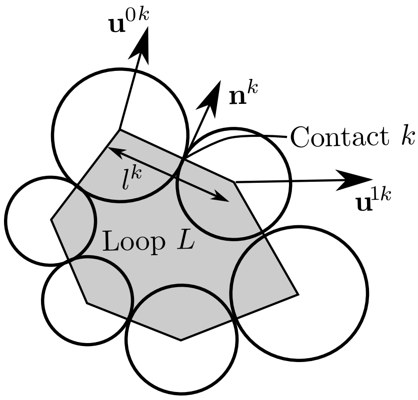

Figure 4: Mesostrain definition of a loop domain L.

in which $\boldsymbol{n}$ is the outer normal to ∂L. At the microscale, the notion of continuous displacement field is meaningless and only grain displacements are known. By assuming a linear interpolation of the displacement along the loop edges, the incremental strain tensor is eventually defined as (see for example Bonelli et al. (2012)):

$$\varepsilon_{ij} = \frac{1}{|L|} \sum_{k=1}^{c} \frac{1}{2} l^k \left(n_j^k \frac{u_i^{1k} + u_i^{0k}}{2} + n_i^k \frac{u_j^{1k} + u_j^{0k}}{2} \right) \tag{3}$$

where $\boldsymbol{u}^{1k}$ and $\boldsymbol{u}^{0k}$ are the incremental displacement of the vertice of k^{th} edge. The notations used in Equation (3) are summarized in Figure 4. In this definition, grain rotations are not taken into account, and the incremental displacement field is interpolated only based on the discrete incremental displacements of grain centers. If grain rotations are considered as the second-order terms of local strain, Equation 3 has to be changed as in Kruyt et al. (2014) for instance. But as shown in the cited paper, the contribution of rotations to the average displacement gradient is negligible for dense granular assemblies.

The spatial distributions of the incremental deviatoric strain for $\varepsilon_{22} = 0.03$ are shown in Figure 5, for both dense and loose specimens. Patterns of diffuse failure (loose specimen) and localized failure (dense specimen) are evident, as exhibited in previous studies (Sibille et al., 2015; Zhu et al., 2016a). Similar to the biaxial simulation in Liu et al. (2018), shear bands with an "X" shape firstly appear in the dense assembly at the stress peak, and then evolves to a diagonal persistent one as shown in Figure 5(a). This evident loss of homogeneity shall induce macroscopic strain softening. Since the domains inside and outside the shear band belongs to different stress states, we investigate their micro- and mesoscopic features individually during Stage III in the following sections. For a quantitative definition of the shear band domain, the reader can refer to Liu et al. (2018).

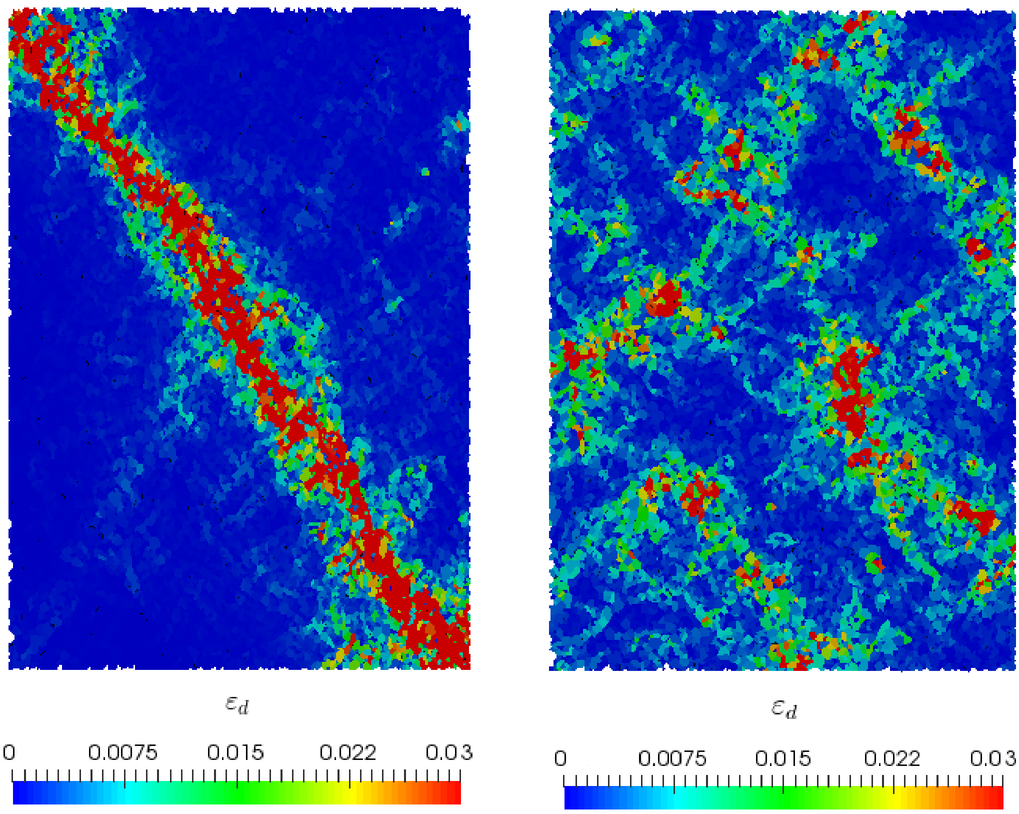

(a) Dense specimen

(b) Loose specimen

Figure 5: Spatial distributions of incremental deviatoric strains ε_d for dense (a) and loose (b) specimens during biaxial tests at $\varepsilon_{22} = 0.03$. Local incremental strains are computed with macroscopic strain increments $\mathrm{d}\varepsilon_{22} = 10^{-3}$.

2.3. *Force chains as stress transmission paths*

As recalled in the introduction, the force chain concept provides a relevant mesoscopic scale to account for the macroscopic mechanical behavior of granular materials (Zhu et al., 2016a; Zhang et al., 2017; Wautier et al., 2017; Tordesillas et al., 2010). The definition of a force chain used throughout this paper is similar to the one proposed by Peters et al. (2005). It is illustrated in Figure 6(a) and briefly reviewed here:

- The particles belonging to a force chain have a larger major principal stress than the mean major principal stress ($\sigma_1 \geq <\sigma_1>$).

- The major principal stress direction of chained particles is aligned with the geometrical direction of contact (less than 45° deviation).

- A force chain contains at least 3 contacting particles.

According to this definition, elementary parts of force chains are composed of groups of three aligned and heavily stressed contacting particles. Such elementary stuctures, referred to as “3-p groups" hereafter, are the simplest mesostructures that can be defined to investigate the stress transmission in granular materials Tordesillas and Muthuswamy (2009)[2]. Attached to each 3-p group, a stress tensor can be defined in quasi-static conditions in the sense of Love-Weber formula (Love, 1927; Weber, 1966; Bagi, 1996; Maeda et al., 2001; Nguyen et al., 2012). By assuming the existence of a micro-stress field, a mesoscopic stress tensor can be defined by averaging this micro-stress over a given domain $\Omega_{\text{3-p}}$ containing the entire 3-p group. If the frontier $\partial\Omega_{\text{3-p}}$ of the domain is chosen such that i) it contains only contact points c_p attached to the 3-p group and ii) at each contact point c_p, the outward normal $\boldsymbol{n}$ to $\Omega_{\text{3-p}}$ equals the contact normal, then the meso-stress $\boldsymbol{\sigma}_{\Omega_{\text{3-p}}}$ reads

$$\boldsymbol{\sigma}_{\Omega_{\text{3-p}}} = \frac{1}{|\Omega_{\text{3-p}}|}\int_{\Omega_{\text{3-p}}} \boldsymbol{\sigma}\, \mathrm{d}S = \frac{1}{|\Omega_{\text{3-p}}|}\int_{\partial\Omega_{\text{3-p}}} (\boldsymbol{\sigma}\cdot\boldsymbol{n})\otimes\boldsymbol{x}\, \mathrm{d}l = \frac{1}{|\Omega_{\text{3-p}}|}\sum_{p}\sum_{c_p}\boldsymbol{F}_{c_p}\otimes\boldsymbol{x}_{c_p} \tag{4}$$

where $\boldsymbol{x}_{c_p}$ is the vector position of contact c_p belonging to particle p and $|\Omega_{\text{3-p}}|$ is the area of domain $\Omega_{\text{3-p}}$. Note that Equation 4 remains valid in 3D by replacing dS and dl with dV and dS respectively. In the above formula, a strong underlying hypothesis is implicitly introduced by imposing locally the mechanical equilibrium (div $\boldsymbol{\sigma} = 0$ and $\sum_{c_p}\boldsymbol{F}_{c_p} = \boldsymbol{0}$). Under this condition, the summations in Equation 4 can be applied to all the contacts included in Ω_{3_p} and not limited to the contacts located on the boundary $\partial\Omega_{\text{3-p}}$.

In the meso-stress definition given in Equation (4), the domain $\Omega_{\text{3-p}}$ has not been specified. As illustrated in Figure 6(b), two particular domains can be considered as:

- the domain $\Omega_{\text{3-p}}^{\text{min}}$ composed of the three grains only (dark domain in Figure 6(b));
- the domain $\Omega_{\text{3-p}}^{\text{max}}$ composed of the three grains and the inner area of the surrounding loops (light and dark domain in Figure 6(b)).

These two domains correspond to the minimal and maximal surface respectively which fulfill the two properties of $\Omega_{\text{3-p}}$ Equation (4). By construction, these two domains give different levels of information in order to describe the stress at the mesoscale:

- $\boldsymbol{\sigma}_{\Omega_{\text{3-p}}^{\text{min}}}$ corresponds to the mean stress tensor inside 3-p groups (only for the solid phase) and provides information about the intensity of the contact forces;

[2]Note that "3-p groups" are considered here instead of the whole force chains for the two following reasons needed for the analyses shown in Section 4: i) these mesostructures are sufficiently simple to be characterized by a single geometric parameter and ii) these mesostructures have better chances to be persistent between to strain increments such that incremental quantities can be defined.

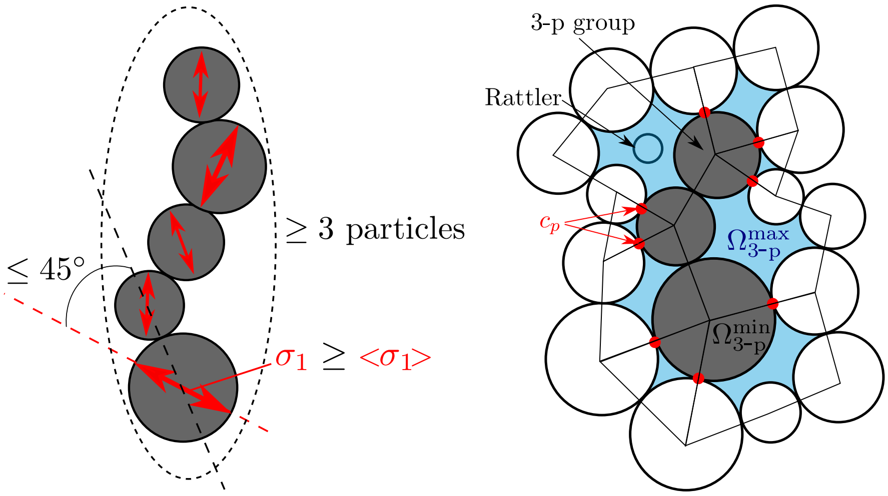

(a) Force chain (b) Mesodomains $\boldsymbol{\sigma}_{\Omega_{3\text{-p}}}$

Figure 6: Definition of (a) a force chain according to Peters et al. (2005) and (b) the two mesodomains $\boldsymbol{\sigma}_{\Omega^{\min}_{3\text{-p}}}$ (3-p group in grey) and $\boldsymbol{\sigma}_{\Omega^{\max}_{3\text{-p}}}$ (3-p group in grey and pore space in light blue). Contact points c_p involved in Equation (4) are shown as red dots.

- $\boldsymbol{\sigma}_{\Omega^{\max}_{3\text{-p}}}$ takes into account the void phase in the stress averaging process and accounts for the local porosity around force chains.

In Figure 7, the strain evolution of the mean deviatoric stresses (over all 3-p groups) computed for $\Omega^{\min}_{3\text{-p}}$ and $\Omega^{\max}_{3\text{-p}}$ are shown for the biaxial test presented in Section 2.1 and compared to the macroscopic deviatoric stress shown in Figure 2. For the dense case, as a shear band appears after the stress peak, averaged mesoscopic stresses are computed separately inside and outside the shear band.

In Figure 7, the qualitative trends observed at the macro and the meso scales are similar. For the dense specimen a stress peak followed by a softening regime is observed for both $\Omega^{\min}_{3\text{-p}}$ and $\Omega^{\max}_{3\text{-p}}$. A better quantitative agreement between meso and macro data is achieved when voids around force chains are taken into account in the meso-stress computation. Indeed, $\boldsymbol{\sigma}_{\Omega^{\max}_{3\text{-p}}}$ incorporates the porous nature of granular materials while $\boldsymbol{\sigma}_{\Omega^{\min}_{3\text{-p}}}$ does not[3]. $\Omega^{\min}_{3\text{-p}}$ and $\Omega^{\max}_{3\text{-p}}$ corresponds indeed to two limit cases for the voids: only solid phase and the solid phase with maximum surrounding void area (see Figure 6(b)). The trend shown by the deviatoric stress computed for $\Omega^{\min}_{3\text{-p}}$ is very informative in the sense that the macro softening results not simply from an increase in the porosity around force chains but also from the decrease in the grain stresses.

[3]It should be underlined that the local porosity corresponding to $\Omega^{\max}_{3\text{-p}}$ is larger than the geometric porosity computed for the whole sample and corresponds to the notion of equivalent porosity (or void ratio) used in soil mechanics to account for the fraction of grain not involved in stress transmission.

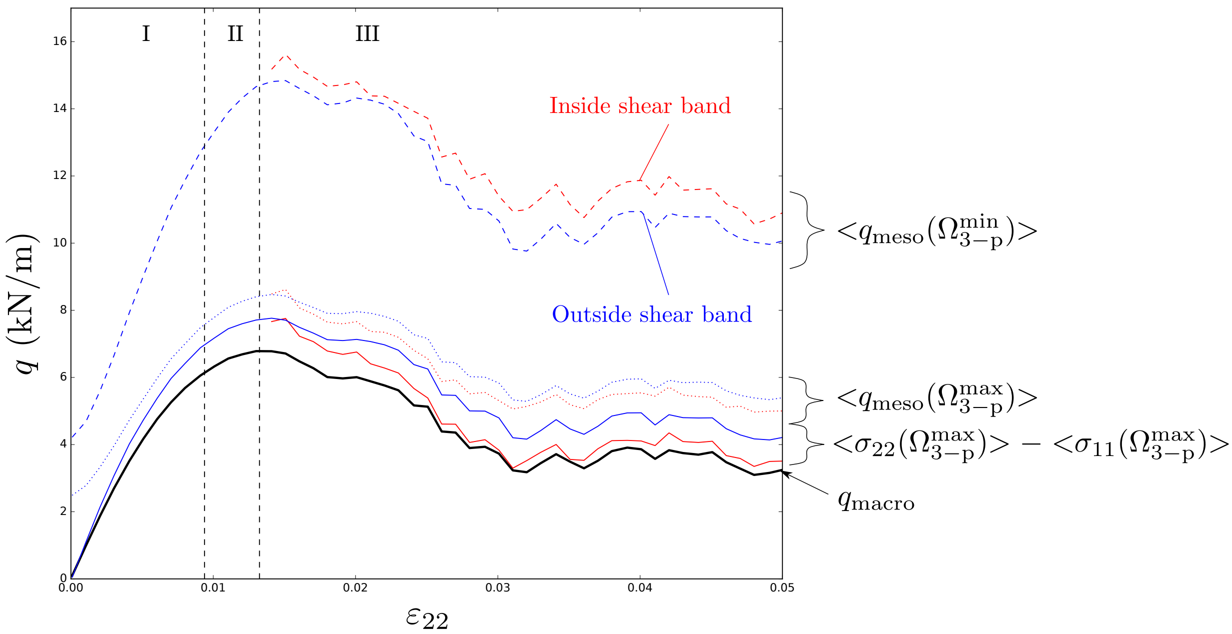

(a) Dense case

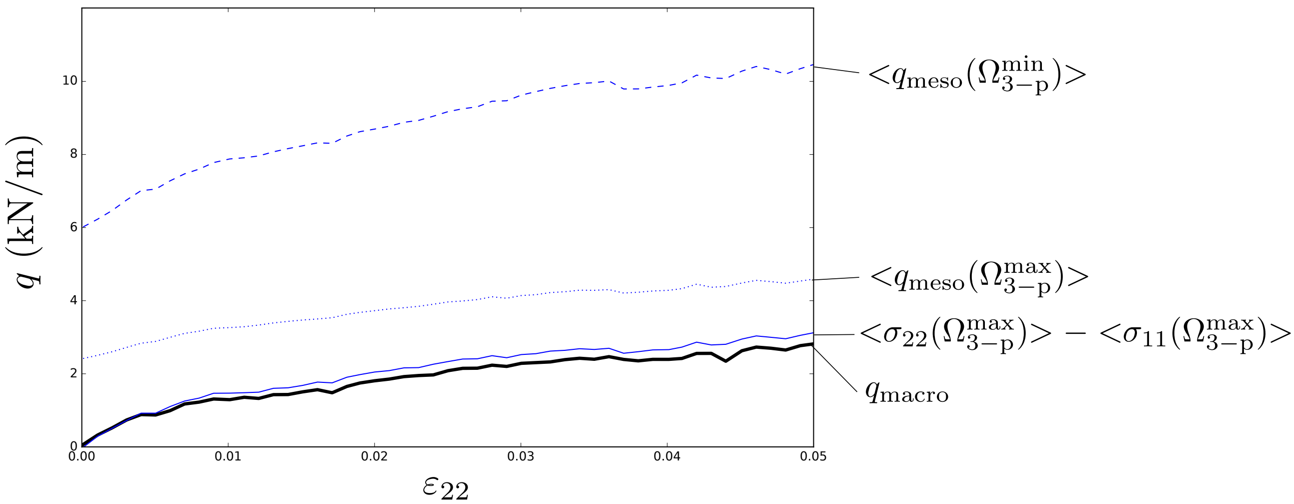

(b) Loose case

Figure 7: Axial strain evolution of the mean deviatoric stresses computed for $\Omega_{\text{3-p}}^{\text{min}}$ and $\Omega_{\text{3-p}}^{\text{max}}$ compared to the macroscale data.

While comparing the mean deviatoric stress noted inside the shear band in Figure 7(a) to the one measured outside it should be noted that $\boldsymbol{\sigma}^{\mathrm{in}}_{\Omega^{\mathrm{min}}_{3-\mathrm{p}}} > \boldsymbol{\sigma}^{\mathrm{out}}_{\Omega^{\mathrm{min}}_{3-\mathrm{p}}}$ while $\boldsymbol{\sigma}^{\mathrm{in}}_{\Omega^{\mathrm{max}}_{3-\mathrm{p}}} < \boldsymbol{\sigma}^{\mathrm{out}}_{\Omega^{\mathrm{max}}_{3-\mathrm{p}}}$. This can be physically interpreted as follows:

- 3-p group density is smaller inside the shear band which results in stress concentration ($\boldsymbol{\sigma}^{\mathrm{in}}_{\Omega^{\mathrm{min}}_{3-\mathrm{p}}} > \boldsymbol{\sigma}^{\mathrm{out}}_{\Omega^{\mathrm{min}}_{3-\mathrm{p}}}$);
- In the meantime, local porosity around 3-p group inside the shear band is higher and counter balances the stress concentration in the solid phase ($\boldsymbol{\sigma}^{\mathrm{in}}_{\Omega^{\mathrm{max}}_{3-\mathrm{p}}} < \boldsymbol{\sigma}^{\mathrm{out}}_{\Omega^{\mathrm{max}}_{3-\mathrm{p}}}$).

In Figure 7, we can observe that the deviatoric meso-stress is non-zero at the initial state, which is due to the fact that the directional information is ignored in the deviatoric meso-stress averaging (q_{meso} is a scalar quantity). The overall average of meso-stesses can be accounted for by computing the deviatoric stress from the mean meso-stress tensor $<\boldsymbol{\sigma}_{\Omega^{\mathrm{max}}_{3-\mathrm{p}}}>$ as $<\sigma^{meso}_{22}> - <\sigma^{meso}_{11}>$ in Figure 7(a).

3. Mesoscopic evolutions: stress, fabric and topology

During the deviatoric loading, macroscopic stress-strain responses are shown in Figure 2. To reveal the underlying mechanisms of the typical Stages I, II and III from new mesoscopic perspectives, this section provides a comprehensive investigation in terms of meso-stress, meso-fabric and topological evolution.

3.1. Chained grain population and meso-stress evolutions

At the first stage of the deviatoric loading of the dense specimen (Stage I), a nearly elastic response with contractancy in volumetric strain is observed in Figure 2. The evolutions of the number of chained particles (the set of particles composing force chains) given in Figure 8 characterize the adaptability of the contact network to the evolving external loading.

In Figure 8, the number of force chain particles increases up to the characteristic point (Stage I) in the dense sample. After the characteristic point (Stages II and III, especially for Stage III), the number of chained particles decreases until reaching a constant value. For the dense specimen, the increasing number of chained particles seems to enhance the strength, as the deviatoric stress increases until Stage II. However, if we consider the loose sample in Figure 8, a weak hardening is accompanied with a decrease in the number of chained particles. This counter intuitive trend may be explained by looking at force chain spatial distributions in Figure 9. As the biaxial loading starts, both the loose

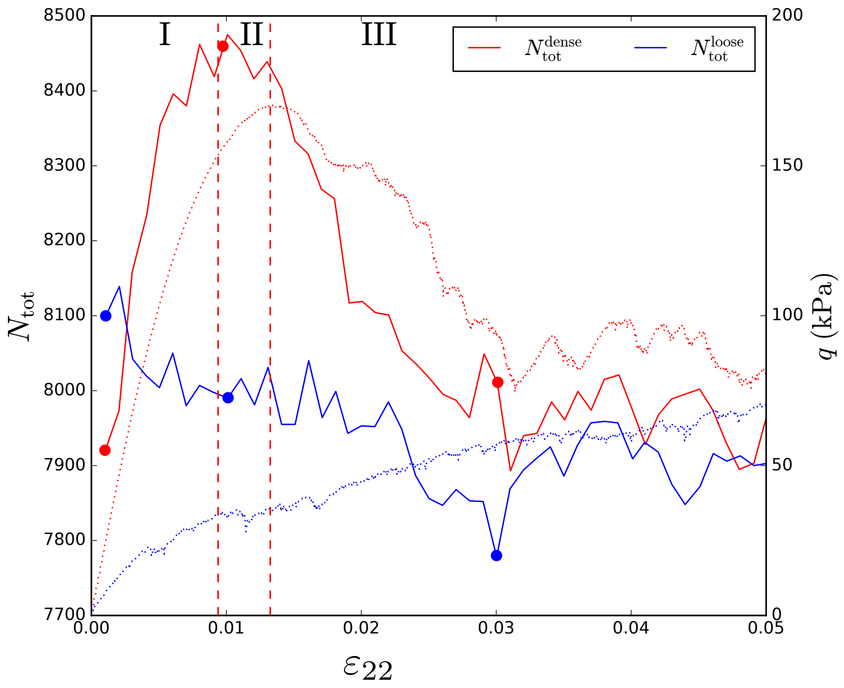

Figure 8: Evolutions of the number of chained particles during biaxial tests for the dense (red) and loose (blue) specimens. The stress-strain macroscopic responses are recalled in dots and the three identified stages for the dense sample are shown with vertical dashed lines. The spatial distributions of chained particles corresponding to the six dot points are given in Figure 9

and dense samples lose horizontal force chains. Thanks to the lateral support of the weak phase, longer and more aligned force chains in the vertical direction are found in the dense sample than in the loose sample (see Figure 9). As a result, the mesoscopic origin of the stress hardening observed in the loose sample corresponds only to the load bearing capacity of preexisting short force chains in the vertical direction while in the dense sample it corresponds to the increase in both the number of chained particles and in the length of force chains as well.

During Stage II for the dense sample, no more particles are recruited to build new force chains but the macroscopic deviatoric stress does not stop rising, which may be due to the fact that at the characteristic point, the existing strong contact network is not yet used at the maximum bearing capacity. As a result, stress concentration within 3-p groups should be observed after the characteristic point.

In Figure 10 the stress concentration phenomenon is quantified by rescaling the mesoscopic deviatoric stress q_{meso} derived from $\boldsymbol{\sigma}_{\Omega_{3\text{-p}}^{\max}}$ (as introduced in Section 2.3) with the macroscopic value q_{macro}. The evolutions of $q_{\text{meso}}/q_{\text{macro}}$ are given for three passing fractions (20%, 50% and 80%) of the cumu-

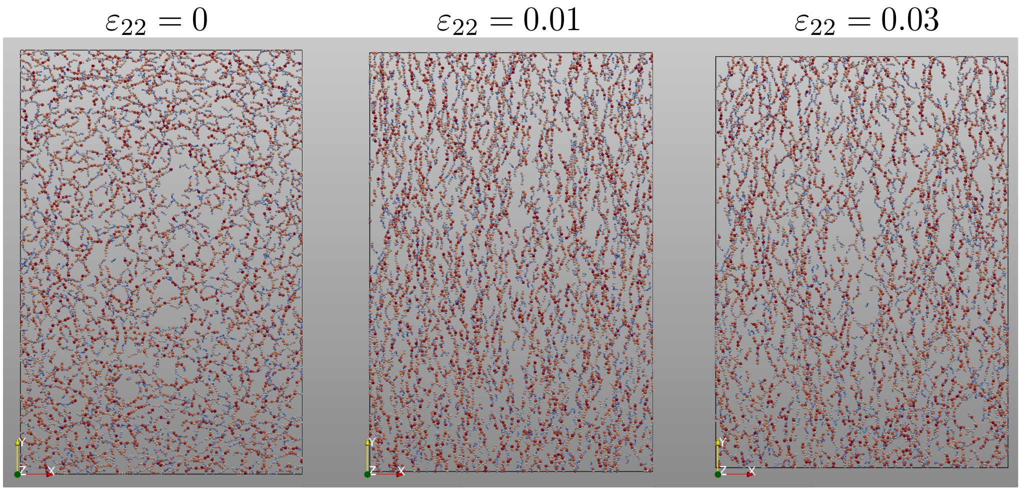

(a) Dense sample

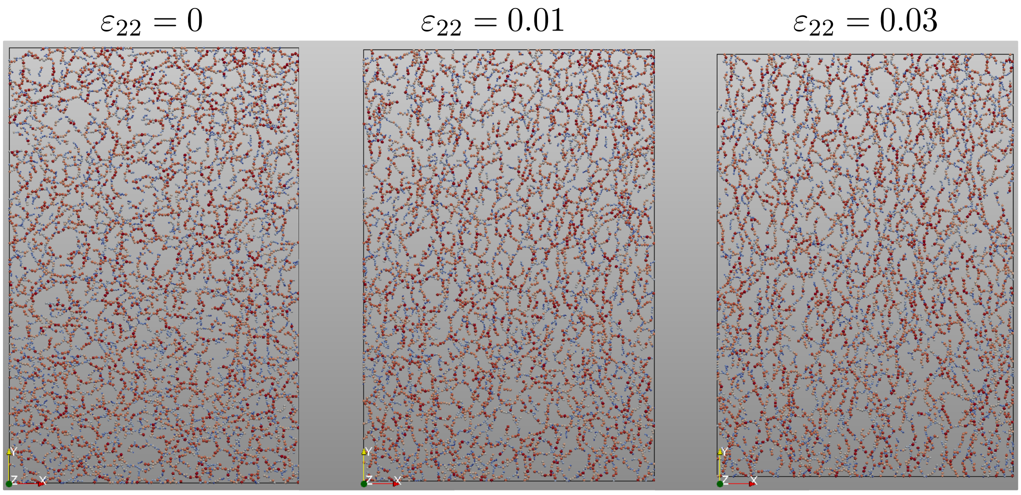

(b) Loose sample

Figure 9: Spatial distributions of chained particles corresponding to the six dot points shown in Figure 8. Particles are colored according to their radius values.

lative distribution curves[4]: $(q_{\text{meso}}/q_{\text{macro}})_{50}$ (median value), $(q_{\text{meso}}/q_{\text{macro}})_{20}$ and $(q_{\text{meso}}/q_{\text{macro}})_{80}$. The statistical distribution of $q_{\text{meso}}/q_{\text{macro}}$ characterizes whether the macroscopic stress is evenly distributed on chained particles while the median value characterizes to which extent stress concentrates in force chains. If only few chained particles contribute to the macroscopic stress, $q_{\text{meso}}/q_{\text{macro}}$ is expected to be quite larger than 1; while if all the particles contribute evenly to the macroscopic stress, $q_{\text{meso}}/q_{\text{macro}}$ is expected to be around unity.

In Figure 10 the ratio $q_{\text{meso}}/q_{\text{macro}}$ decreases until $\varepsilon_{22} = 0.01$ (the hardening regime) before increasing again in stage II and III, which corresponds to stress concentration in force chains during the

[4]The cumulative distributions of $q_{\text{meso}}/q_{\text{macro}}$ are not shown here, but they experience similar shapes as the rotation distribution for 3-p groups (see in Section 4, Figure 20).

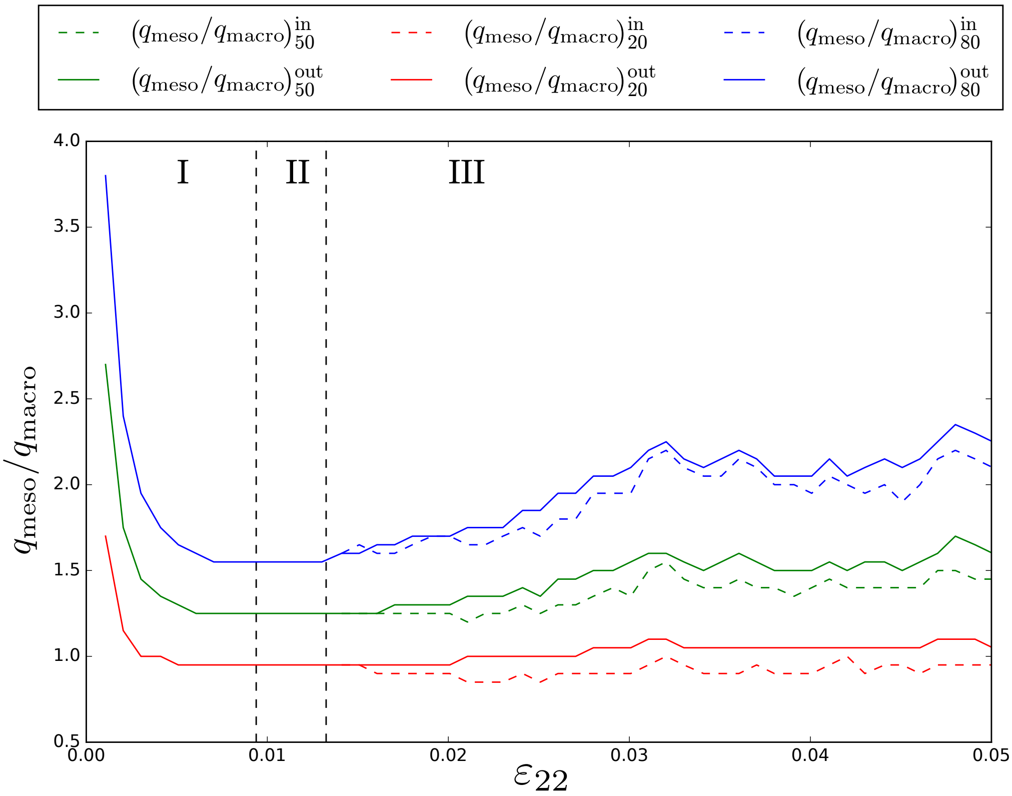

Figure 10: Evolution of the 20 % (lower), 50 % (middle) and 80 % (upper) passing fractions of the cumulative distribution of $q_{\mathrm{meso}}/q_{\mathrm{macro}}$ during biaxial loading for the dense specimen. After the stress peak, cumulative distributions are computed separately inside (dashed) and outside (solid) of the shear band. q_{meso} is computed based on $\boldsymbol{\sigma}_{\Omega^{\max}_{3\text{-p}}}$ (see Section 2.3)

softening regime. These observations are consistent with Figure 8 and 9 showing that the number of chained particles increases during Stage I (the macroscopic load is distributed among an increasing number of chained particles), and decreases in Stages II and III (the macroscopic load becomes more and more concentrated on the remaining 3-p groups as the number of chained particles decreases rapidly).

The stress concentration phenomenon is also consistent with the differences in deviatoric meso-stresses inside and outside the shear band observed in Figure 7(a). When the local porosity is not taken into account, the deviatoric meso-stress inside the shear band shows a higher magnitude.

3.2. Mesoscale fabric

At the contact level, the non-directional connectivity of a network can be assessed through the coordination number. For the whole contact system, $Z_c^{tot} = 2N_c/N_p$, where N_c is the total number of contacts within the overall system, and N_p is the total number of particles. Moreover, the contact system without rattlers (particles with no contact) should also be concerned, to better show the average transmission path of loaded particles. The coordination number disregarding the rattlers is calculated as $Z_c^{nonFree} = 2N_c/(N_p - N_{free})$, where N_{free} denotes to the number of rattlers. In Figure 11, coordination number for all contacts Z_c^{tot} and for the contact system without rattlers $Z_c^{nonFree}$ are shown, together with the volumetric strain evolution. The decreasing trend of coordination number is identified for all the three periods (I, II, III) for the dense specimen, while the loose specimen seems to gain more contacts during the loading process. A significant feature is that the coordination number drops during Stage I for the dense specimen despite the contractant behavior and an increase in the number of chained particles. As already shown by Kruyt and Rothenburg (2016), this can be explained by the anisotropy of the contact network which increases in the vertical direction during Stage I. The coordination number as a scalar information is not sufficient to describe or explain the hardening phase with contractancy in dense granular materials.

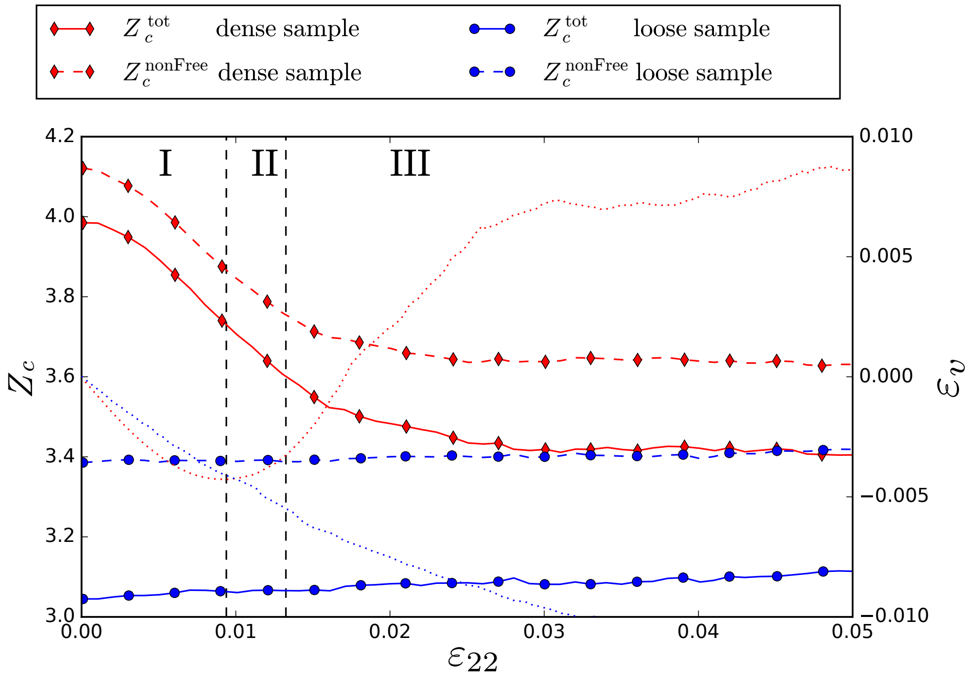

Figure 11: Mean coordination numbers computed for all particles (solid) and for non-rattlers (dashed) over the whole sample domain. The evolutions are given for the dense (red diamonds) and the loose (blue dots) specimens during the biaxial test. The volumetric strain curves are recalled in dotted lines.

Considering the contact orientation characteristics, the fabric tensor of granular contact system was introduced (Oda, 1982; Satake, 1982) and widely applied in anisotropy analysis. The concept of fabric in granular materials is quite important for describing the statistical and geometrical information of the structure, and it has also been incorporated in some modified constituitive models (Li and Dafalias, 2012; Dafalias, 2016). The contact-based anisotropy provides the complementary information to the global loss of contacts and force chain population evolution, for both the hardening and softening phases. As commonly used, the second-order fabric tensor $\boldsymbol{F}$ within granular assembly is averaged by contact normals within a system:

$$\boldsymbol{F} = \frac{1}{N_c} \sum_{c=1}^{N_c} \boldsymbol{n}^c \otimes \boldsymbol{n}^c \tag{5}$$

where the $\boldsymbol{n}^c$ is the contact normal vector. Usually, this fabric tensor $\boldsymbol{F}$ is analyzed on the whole contact system ($c \in [1, N_c]$) and is proved to be one of the contributions to the stress anisotropy (Rothenburg and Bathurst, 1989; Li and Yu, 2013; Guo and Zhao, 2013). To distinguish the role of strong and weak contact systems, the anisotropy evolutions of different contact systems were shown in Guo and Zhao (2013). Particularly, for a single force chain k, the same formal expression as Equation 5 could also be adopted. The corresponding fabric tensor $\boldsymbol{F}^k$ is then fully characterized in 2D by the major direction θ_k and eigen values $F^k_\pm$:

$$tan(2\theta_k) = \frac{2F^k_{12}}{F^k_{11} - F^k_{22}} \tag{6}$$

$$F^k_\pm = \frac{1}{2}(F^k_{11} + F^k_{22}) \pm \sqrt{(\frac{1}{2}(F^k_{11} - F^k_{22}))^2 + (F^k_{12})^2} \tag{7}$$

For a given force chain k, the deviatoric invariant (second invariant of the deviatoric part of the fabric tensor) $D_k = F^k_+ - F^k_-$ characterizes the recti-linearity of the mesostructure, while θ_k provides an estimation of the force chain orientation. By definition, $D_k \in [0, 1]$ with $D_k = 1$ corresponding to a perfectly straight force chain and $D_k = 0$ to a sort of "isotropic" force chain (very tortuous in other words). Figure 12 gives these two extreme conditions of force chain linearity. Usually, according to the definition of force chains given in Section 2.3, the maximum deviation angle for each 3-p group is 45 °. This geometrical limit results in D_k larger than 0.5 in most cases.

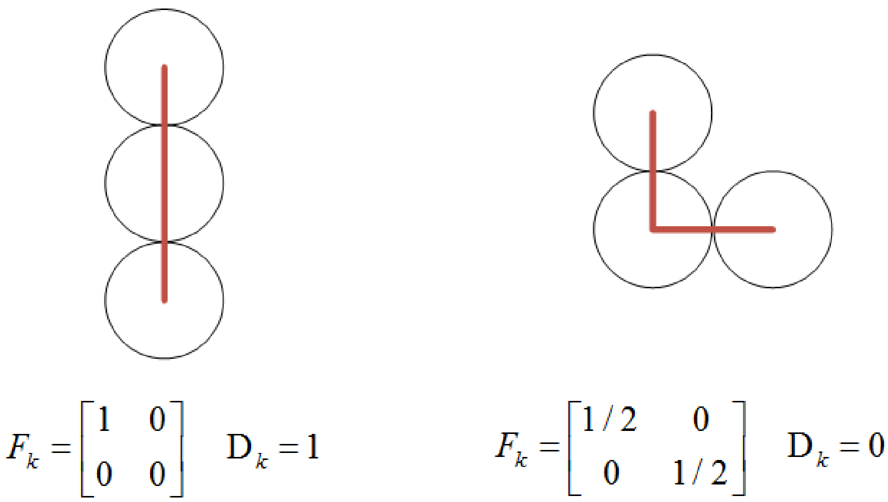

Figure 12: Extremal conditions of force chain linearity D_k.

Similarly, the deviatoric invariants D and D_s corresponding to the overall fabric tensor $\boldsymbol{F}$ (considering contacts within the whole sample) and to the fabric tensor $\boldsymbol{F_s}$ built only from the chained contacts can be defined. Figure 13(a) shows the evolutions of D, D_s and $<D_k>$ (the average D_k over all force chains) during the biaxial loading, and Figure 13(b) gives the schematic drawing of the difference between D_s and D_k. $<D_k>$ increases and reaches a maximum level at the end of Stage I, indicating that force chains become more and more linear during this period. At the same time, D_s rises from 0 to around 0.6 and D increases with a weaker trend. It is accepted that the strong contact system plays an important role in fabric anisotropy generation (Radjai et al., 1998; Guo and Zhao, 2013), and the increase in force chain recti-linearity and force chain population during Stage I both reflect that fact. $<D_k>$ and D_s reach their maximum levels around the characteristic point (dividing line between Stage I and II), while the overall fabric invariant D reaches its maximum even after the stress peak (at the beginning of Stage III). Indeed during Stage II, the overall anisotropy increases due to the weak contact phase. By combining these observations with stress concentration results from Figure 10, it can be inferred that:

- The first stage of hardening is associated with a strong increase in fabric anisotropy and proportions of strong contact phase (force chains);
- The hardening with dilatancy (Stage II) corresponds to the beginning of load concentration and to the increase in weak contact anisotropy;
- During the softening phase, the mesoscopic fabric anisotropy related to the force chain recti-linearity decreases in general, leading to the axial stress reduction.

3.3. Topological and geometrical exchanges

Introduced in Section 2.3, 3-p groups are the elementary parts composing force chains responsible for stress transmission. Their geometric evolutions are strongly coupled with the deformability of the grain loops surrounding the force chains. These loops can change either in topology (coordination number) or in geometry (area). For a given loop, the change in topology can be divided in three categories: (a) keep the same particles and contacts, i.e, unchanged in topology, called “C-loop”; (b) lose one or several contacts and become larger, called “L-loop”; (c) create new contacts among the particle participants and get smaller cells, called “S-loop”. Possible topological exchanges of “L-loop”, “C-loop” and “S-loop” are illustrated in Figure 14.

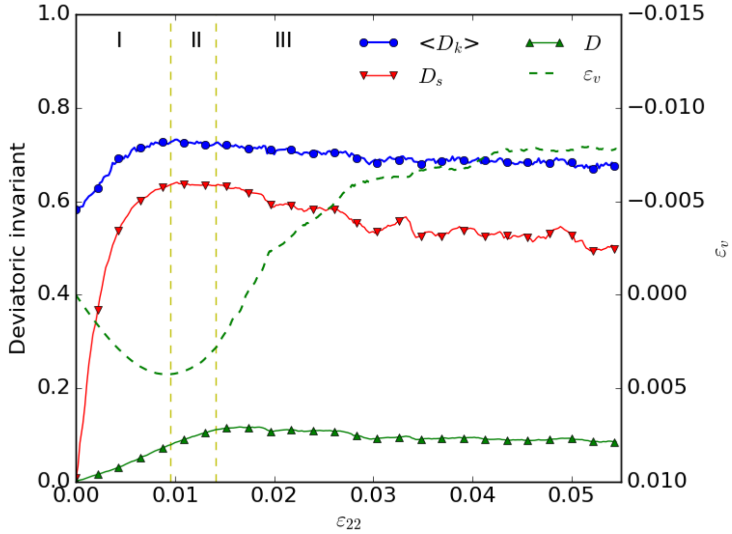

(a)

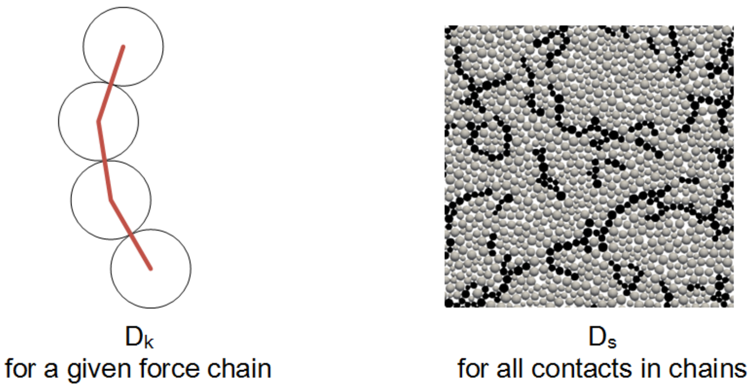

(b)

Figure 13: Force chain linearity compared with the anisotropies of force chain network and the overall contact network. Quantities are computed over the whole sample domain. The evolution curves are shown in (a), and the sketches for how to calculate D_k and D_s are shown in (b).

Around each 3-p group, there exists dozens of loops which could be identified as “C-loop”, “S-loop” or “L-loop”. The average fractions of the three topological exchanges related to each 3-p group are plotted in Figure 15. The exchanges are defined incrementally for strain increments of 0.1 %. From the beginning to the end, the set of “C-loop” around 3-p groups represents the largest population (over 90%). The set of “L-loop” represents a larger proportion than “S-loop” before the stress peak ($\varepsilon_{22} = 0.014$), which is consistent with the decrease in coordination number shown in Figure 11. Therefore during the hardening phase, several contacts are opened to form larger loops, which contributes to fabric anisotropy. As the shear band forms after the stress peak, topological exchanges concentrate inside the shear band where the fraction of “C-loop” decreases significantly.

In Figure 15, “L-loop” represents a larger proportion than “S-loop” during the hardening phase

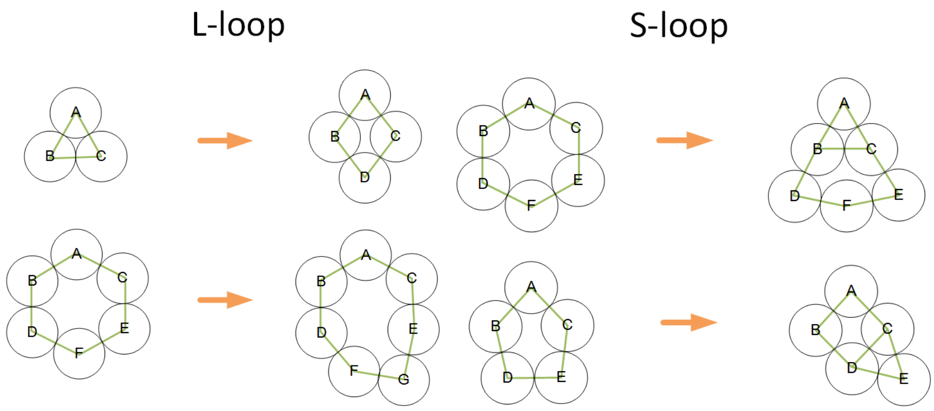

(a) (b)

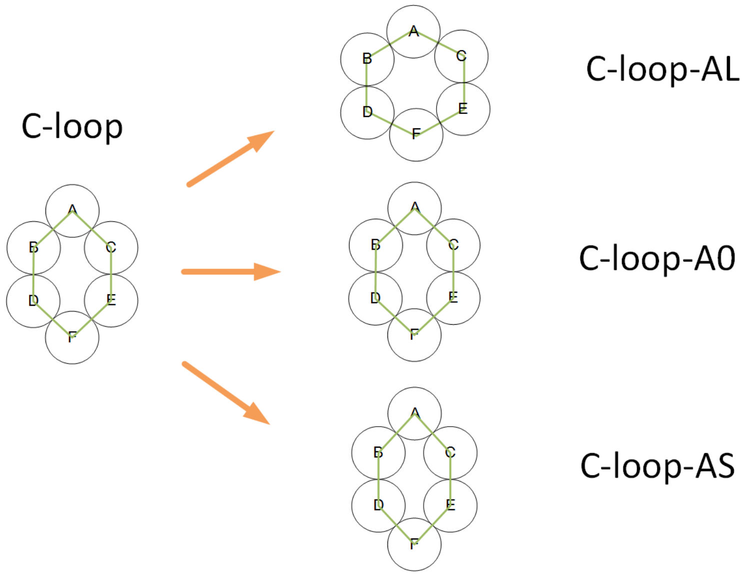

(c)

Figure 14: Possible changes for 2D loops between steps: (a) "L-loop": loops will be enlarged in topology; (b) "S-loop": loops will shrink in topology; "C-loop": loops will keep the same topology, composed by "C-loop-AL" (larger area in next step), "C-loop-A0"(same area in next step) and "C-loop-AS"(smaller area in next step).

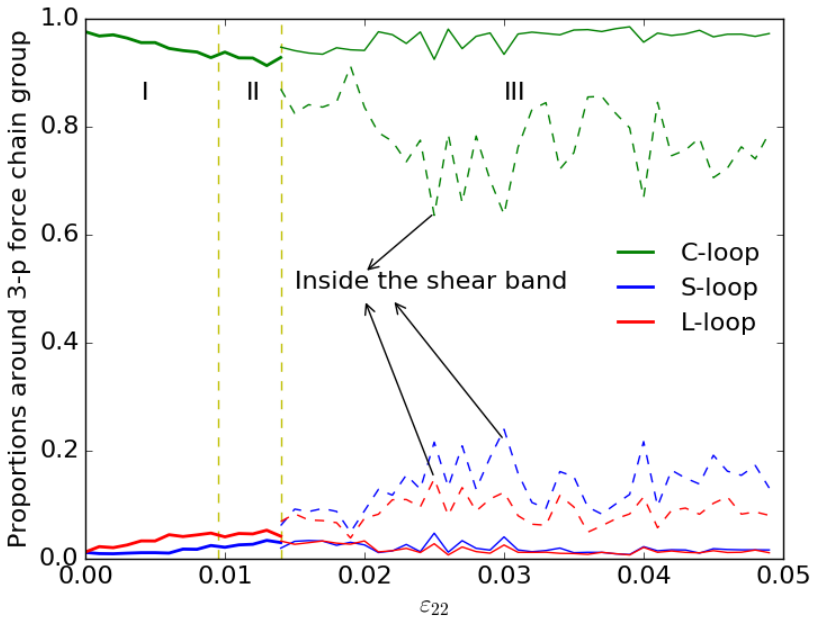

Figure 15: Proportions of topological loop exchanges around 3-p force chain groups. During Stage III, the dashed line shows the corresponding evolutions inside the shear band, while the solid line shows those outside the shear band.

(Stage I and II). These topological exchanges tends to indicate a dilatancy trend, however the volumetric strain does not behave like that during Stage I. To have a rational explanation of this inconsistency, it is necessary to look at the area changes for the topologically constant loops. As a result, "C-loop" can be redivided into "C-loop-A0", "C-loop-AS" and "C-loop-AL" to represent loops with unchanged area, smaller area and larger area respectively, as shown in Figure 14(c). Figure 16 gives the evolutions of average proportions of "C-loop-A0", "C-loop-AS" and "C-loop-AL" around 3-p groups (solid line) and for the whole system (dashed line). It can be seen that the crossing points of proportion curves "C-loop-AS" and "C-loop-AL" are near to the characteristic point $\varepsilon_{22} = 0.01$, before which the "C-loop-AS" owns a larger fraction (nearly Stage I). This is the mesoscopic origin of the contractive behavior observed at first stage of hardening (Stage I). During this period, the loop exchanges (or contact loss and gain) do not influence very much on the volumetric evolutions, but the area evolutions of "C-loop" induce the contractancy hardening features. During Stage II, both topological exchanges (Figure 15) and area evolutions (Figure 16) indicate a dilative trend, which gives corresponding trends compared to the volumetric strain in Figure 2. Another interesting observation in Figure 16 is that the crossing point for 3-p groups comes earlier than for the whole system which denotes once again the driving role played by the surrounding voids around force chains in Figure 6(b). In Zhu et al. (2016b), loops surrounding force chains were also investigated, especially the transformation from L3 (loops of 3 particles) to L6 (loops of 6 particles) was focused on. It

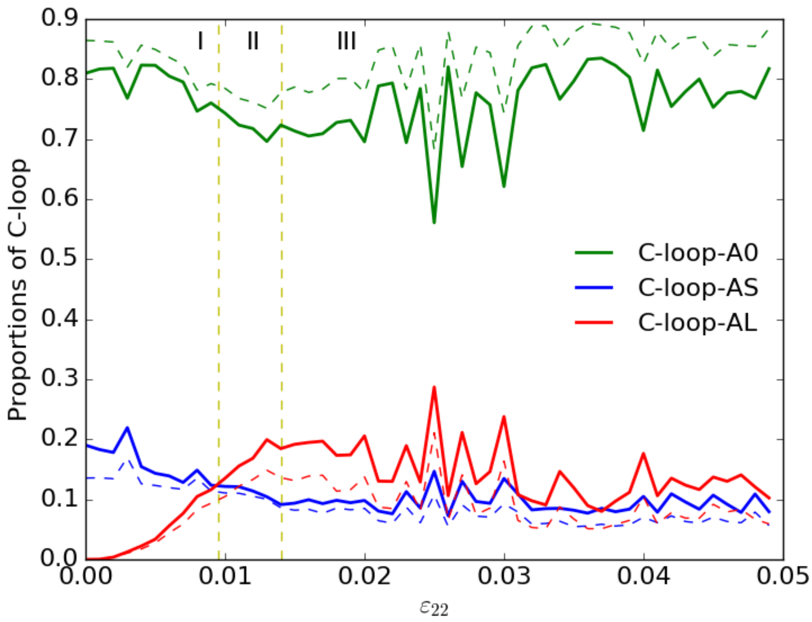

Figure 16: Proportions of "C-loop" with different area changes: around 3-p force chain group (solid line); for the whole system (dashed line).

was proved that geometrical and topological evolutions of loops surrounding force chains could be regarded as the key origin of the overall stress-strain responses in granular materials. This paper considers in a more general way by incorporating transformation types of all loops within the granular assembly, and combined to the results of defined mesoscopic stress and the force chain recti-linearity, the hardening phases with both the contractancy and dilatancy are further figured out.

In summary, we can conclude that the loop topology evolution and the area change of topologically constant loops play different roles in hardening phases. As the loop size and area both increase during Stage II, kinematic constraints around force chains are released and force chains are prompt to be destabilized, which could finally induce the softening process.

4. 3-p group bending and rotation in relation with macroscopic softening

The geometry of a 3-p group can be characterized by the two angles α_1 and α_2, as shown in Figure 17. Equivalently, the bending angle $\beta = |\alpha_1 - \alpha_2|$ and the mean orientation angle $\gamma = \frac{1}{2}(\alpha_1 + \alpha_2)$ can be considered. In addition to these angles, the principal stress orientation (as defined by diagonalizing $\sigma_{\Omega_{3\text{-p}}}$) is characterized by a third non coaxiality angle θ (Figure 17).

This section focuses on the relations between the geometric evolutions of 3-p groups (characterized by the orientation angle γ and the bending angle β) and the associated meso-stresses (characterized by the non coaxiality angle θ defined in Section 2 and the deviatoric meso-stress defined in

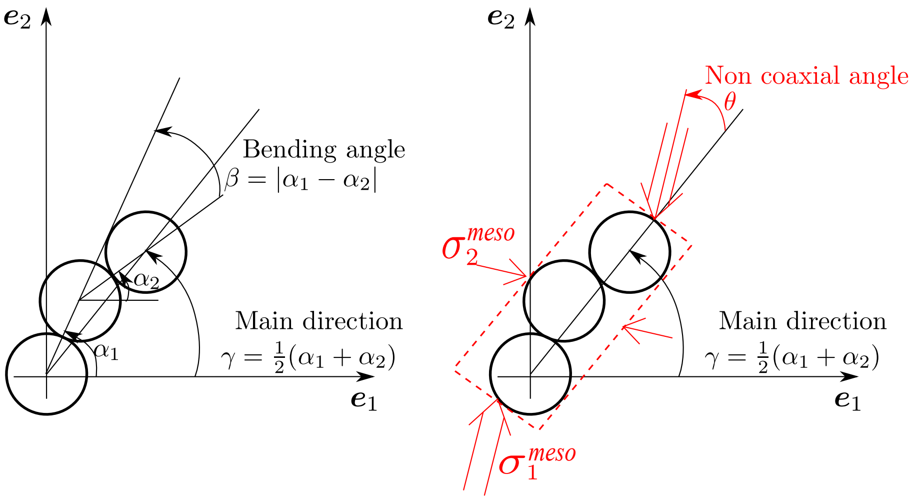

Figure 17: Geometrical and mechanical features of 3-p groups. The geometry is characterized by the bending angle β and orientation angle γ while the mesoscopic stress state is characterized by the major (σ_1) and minor (σ_2) stresses as well as the non coaxial angle θ.

Equation (4) for $\Omega_{\text{3-p}}^{\min}$).

4.1. Force chain bending and buckling

In the wake of previous researches, e.g. Tordesillas (2007); Zhu et al. (2016b); Zhang et al. (2017), it is tempting to relate internal deformation of 3-p groups (in the form of bending) to force chain buckling (mesoscopic softening) and thus to macroscopic softening. In most of existing studies, buckling is defined as an increase in the bending angle β (see Figure 17). However, a rigorous definition of buckling needs to incorporate both a geometrical evolution and a force or stress saturation or decrease. As a result, a distinction is emphasized here between *bending* ($\mathrm{d}\beta > 0$) and *buckling* which should incorporate an additional decreasing load information in usual definitions found in the literature.

To this respect, a possible mesoscale definition is to relate the bending of a 3-p group during the biaxial loading ($\frac{\mathrm{d}\beta}{\mathrm{d}\varepsilon_{22}} > 0$) to a simultaneous decrease in the deviatoric stress derived from $\boldsymbol{\sigma}_{\Omega_{\text{3-p}}^{\max}}$ ($\frac{\mathrm{d}q_{\text{meso}}}{\mathrm{d}\varepsilon_{22}} < 0$). Mathematically speaking a buckling definition is sought when both the conditions are reached:

$$\frac{\mathrm{d}\beta}{\mathrm{d}\varepsilon_{22}} > 0, \qquad \text{and} \qquad \frac{\mathrm{d}q_{\text{meso}}}{\mathrm{d}\varepsilon_{22}} < 0 \tag{8}$$

In Figure 18, the spatial distribution of $\frac{\mathrm{d}\beta}{\mathrm{d}\varepsilon_{22}}$ and $\frac{\mathrm{d}q_{\text{meso}}}{\mathrm{d}\varepsilon_{22}}$ is illustrated for two axial strain values (at the peak and in the softening regime). In this figure, the size of the symbols is proportional to the absolute variation of the deviatoric stress $|\frac{\mathrm{d}q_{\mathrm{meso}}}{\mathrm{d}\varepsilon_{22}}|$. Triangles pointing upward correspond to 3-p groups with increasing deviatoric stress while triangles pointing downward correspond to 3-p groups with decreasing deviatoric stress. 3-p groups undergoing bending are highlighted in dark. As a result, 3-p groups that fulfill the buckling definition of Equation 8 correspond to dark triangles pointing downward in Figure 18.

In Figure 18, the largest evolutions in $|\frac{\mathrm{d}q_{\mathrm{meso}}}{\mathrm{d}\varepsilon_{22}}|$ (shown here) and in $|\frac{\mathrm{d}\beta}{\mathrm{d}\varepsilon_{22}}|$ (not shown here) concentrate in the shear band domain. Since 3-p groups are elementary parts constituting force chains, a strong spatial correlation is observed between adjacent 3-p groups in terms of deviatoric stress rate (adjacent triangles are of similar sizes). It is however not always the case for bending rate. In particular, 3-p groups subjected to a decrease in deviatoric stress and in bending angle (light triangles pointing downward) are often located in between 3-p groups subjected to a decrease in deviatoric stress together with an increase in bending angle (dark triangles).

As a result, and contrary to what is usually stated in the literature, 3-p groups are not the right elementary structure to define buckling at the mesoscopic scale. As illustrated in Figure 19, we can find indeed geometrical configurations in which a given 3-p group undergoes bending ($\frac{\mathrm{d}\beta}{\mathrm{d}\varepsilon_{22}} > 0$) while the next 3-p group in the same force chain experience an opposite straightening evolution ($\frac{\mathrm{d}\beta}{\mathrm{d}\varepsilon_{22}} < 0$). These two geometric evolutions are indeed a consequence of grain rolling (between chained grains, sliding is unlikely to occur simply by definition of a force chain). Despite having two opposite geometrical evolutions, the two 3-p groups have very similar meso-stress tensor because of spatial correlation (Frenning and Alderborn, 2005). Therefore, for a given meso-stress evolution, both bending and straightening can be observed simultaneously. For 3-p groups, the buckling condition considering β variations is thus not relevant and a proper definition should be sough while considering larger mesostructures. 3-p groups can however still be used to analyze the impact of force chain rotations onto the macroscopic behavior which is detailed in Section 4.2.

4.2. 3-p group rotations inside and outside shear band

Cumulative distributions of γ for three particular states are shown in Figure 20. In the coordinate system recalled in Figure 17, 90° denotes a vertical direction aligned with the macroscopic loading direction (e_2).

In the initial state (Figure 20(a)), the cumulative distribution of γ is typical of a uniform distribution between 0 and 180° which is consistent with the isotropic stress state imposed before any biaxial loading and the spatial distribution of chained particles illustrated in Figure 9. As soon as the load

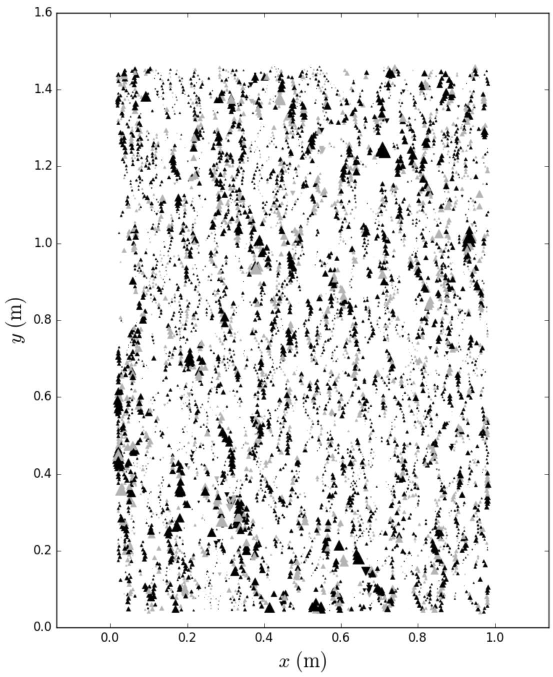

(a) Dense sample, $\varepsilon_{22} = 0.010$

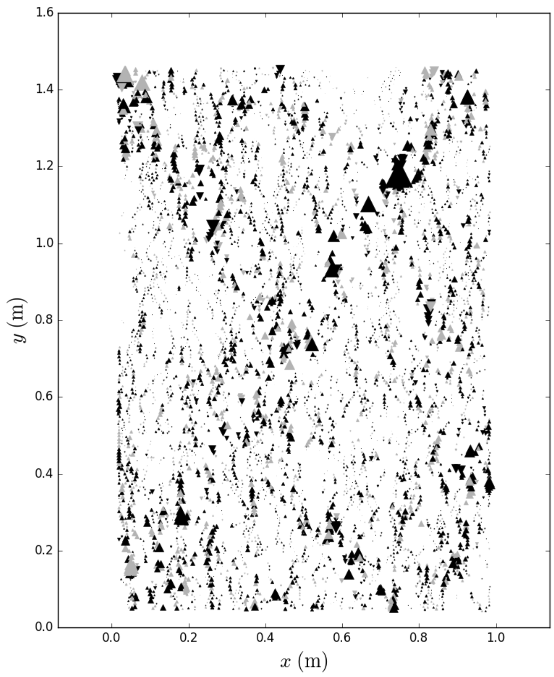

(b) Dense sample, $\varepsilon_{22} = 0.013$

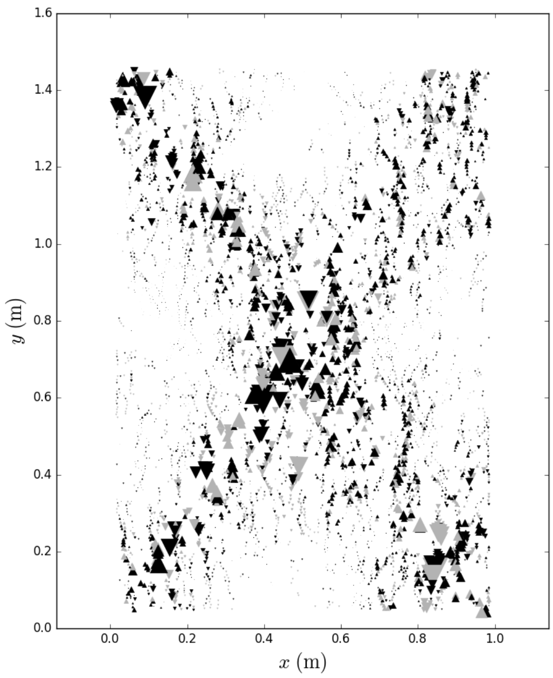

(c) Dense sample, $\varepsilon_{22} = 0.015$

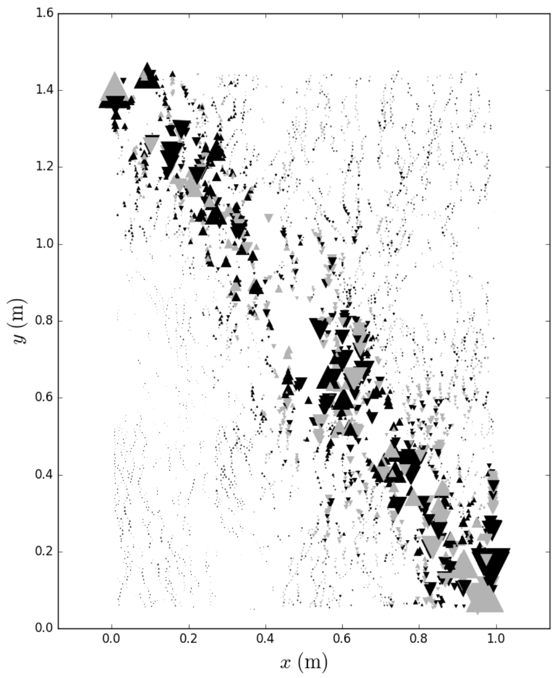

(d) Dense sample, $\varepsilon_{22} = 0.025$

Figure 18: Spatial distribution of deviatoric stress rates in 3-p groups for different axial strain levels in the dense sample. The size of the symbols is proportional to the absolute variation of the deviatoric stress $|\frac{\mathrm{d}q_{\mathrm{meso}}}{\mathrm{d}\varepsilon_{22}}|$. Triangles pointing upward correspond to 3-p groups with increasing deviatoric stress and vice versa. 3-p groups undergoing bending are shown in dark.

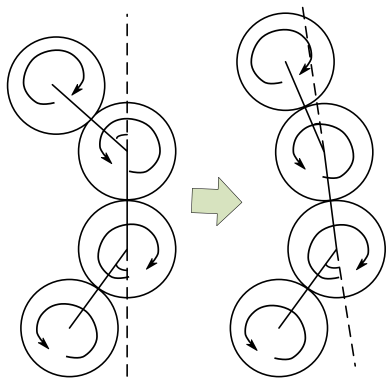

Figure 19: Example of simultaneous bending and straightening for two neighboring 3-p groups.

progresses, the force chain orientation changes ($\varepsilon_{22} = 0.01$, Figure 9). The cumulative distribution shows a concentration of 3-p groups with mean orientation around 90° in Figure 20(b) (which is consistent with qualitative observations of Figure 9). After the shear band has formed, three cumulative distributions can be considered in Figure 20(c) for i) the domain inside the shear band, ii) the domain outside the shear band and iii) the whole sample. For the whole domain, γ is still aligned with the vertical direction on average, but slight deviations are observed while restricting the analysis inside and outside the shear band as illustrated in Figure 20(c) and 20(d):

- inside the shear band γ tends to align to a direction less than 90°, denoting a clockwise rotation;
- outside the shear band γ shows the opposite trend, the counter clockwise rotation is identified.

To better show this trend, the strain evolution of the cumulative distribution is shown in Figure 21 in the same form as used in Figure 10. Values corresponding to 20 % (γ at Point A in Figure 20), 50 % (γ at Point O in Figure 20) and 80 % (γ at Point B in Figure 20) passing fraction of γ cumulative distributions are plotted together in Figure 21. Force chain geometrical directions of all passing percentages follow the same trend with clockwise rotaion inside the shear band and counter-clockwise rotation outside the shear band (as illustrated in Figure 20(d)).

Note that the rotation of force chains here is not the same indicator as in previous studies. For example, Oda and Kazama (1998); Iwashita and Oda (2000) used individual particle rotations to identify fluctuation behaviors inside the shear band. Tordesillas et al. (2014, 2016) gave a vortex definition based on particle displacement field and explored the relations between vortices and force chain buckling. Kawamoto et al. (2018) found that major principal stress inside the shear band rotates differently compared to the major principal stress outside the shear band. The original signature of force chain geometrical rotation introduced in this paper corresponds to the rotation of mesostructures

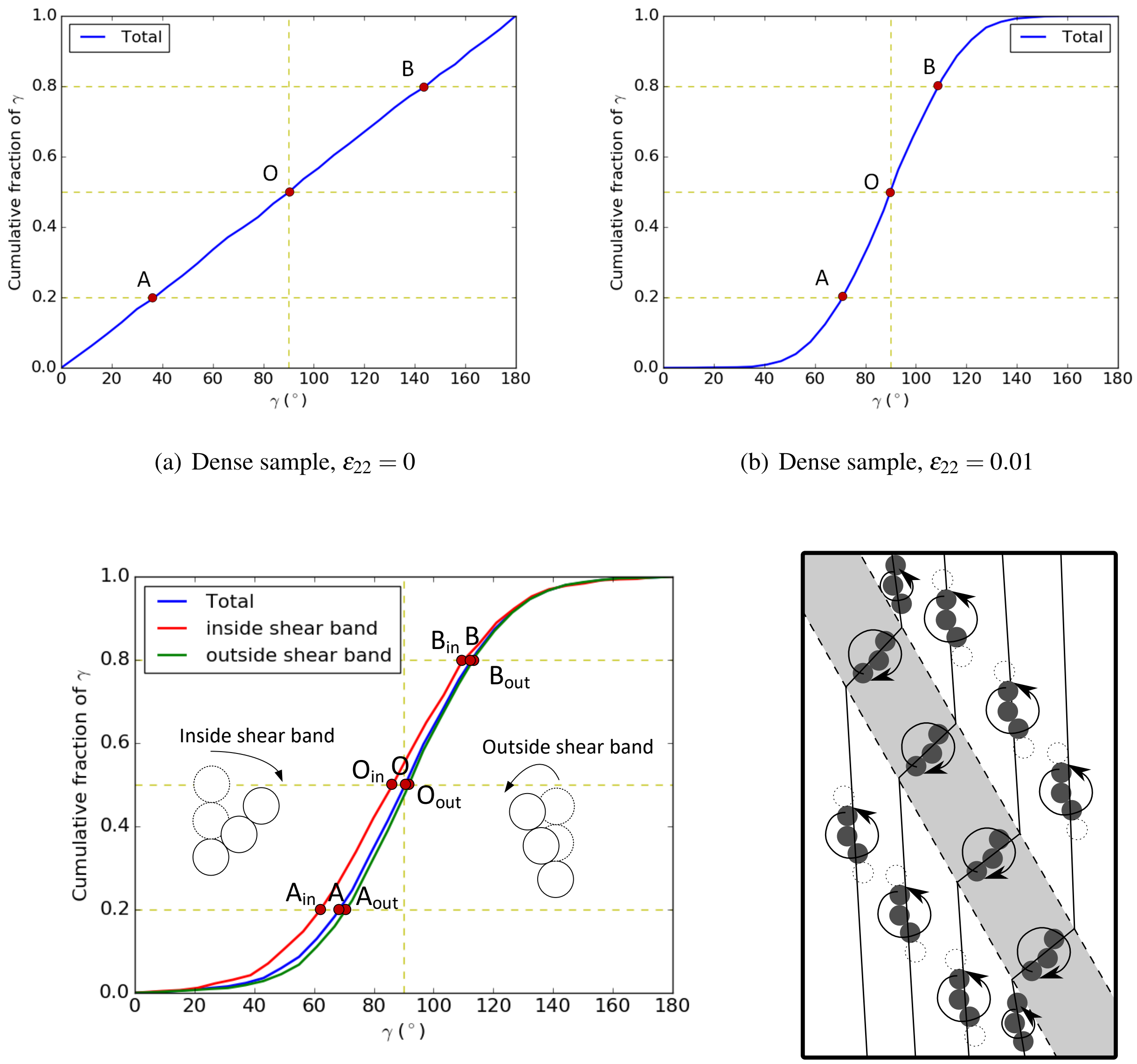

(a) Dense sample, $\varepsilon_{22} = 0$

(b) Dense sample, $\varepsilon_{22} = 0.01$

(c) Dense sample, $\varepsilon_{22} = 0.04$

(d) 3-p groups rotations (Stage III)

Figure 20: γ cumulative distributions for three strain levels within the dense sample: (a) initial state; (b) characteristic state; (c) fully developed shear band state. (d) schematic diagram showing 3-p group rotations probably responsible for macroscopic softening.

of a few grains, while the internal changes (such as displacement of each sphere) within the 3-p group are ignored.

In Tordesillas et al. (2016), the force chains are almost at the boundary of the vortices. Indeed, the geometrical rotation of force chains influences the surrounding particles and the confining loops. As a result, displacements and rotations of particles on both sides of a given force chain may differ and form structures like vortices. Because the rotation of 3-p group is more intense inside the shear band, more vortices are identified within the shear band zone which is consistent with the results of Tordesillas et al. (2016).

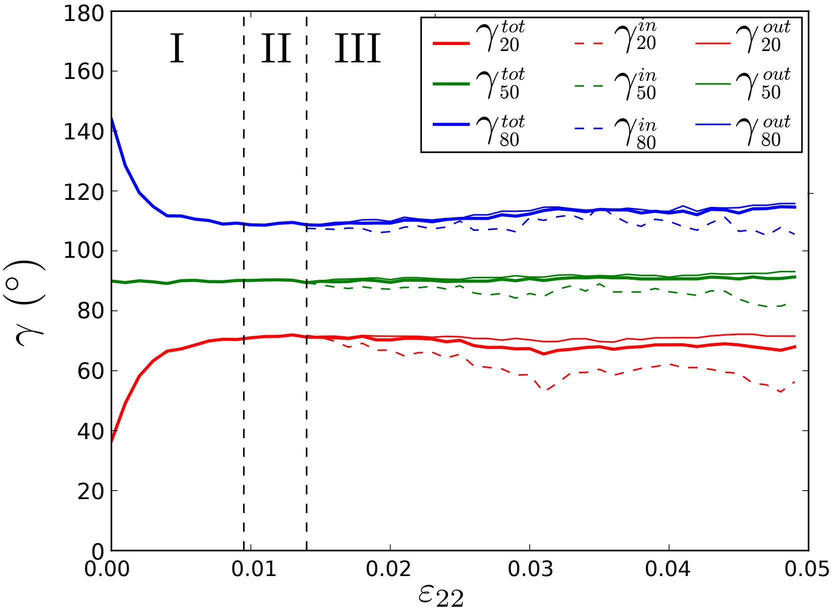

Figure 21: Strain evolution of the 20 %, 50 % and 80 % passing fractions of the cumulated distributions of the geometrical orientation γ of 3-p groups. After the stress peak, cumulative distributions are computed separately inside and outside the shear band.

4.3. Principal meso-stress rotations in force chains

Besides the geometrical rotation, a similar analysis can be carried out for the principal mesoscopic stress rotation as shown in Figure 22 for the angle $\gamma + \theta$. Stress also rotates in opposite directions inside (clockwise) and outside (counter clockwise) the shear band. A small difference is that principal stress orientations show less fluctuations around 90° as $(\gamma+\theta)_{80} - (\gamma+\theta)_{20} < \gamma_{80} - \gamma_{20}$. This means that the stresses of 3-p groups are on average more aligned with the axial loading direction than the geometrical orientation.

We do recall that, internal geometrical changes are induced by the evolution in the external forces applied to the 3-p groups. As a result the geometrical rotation of 3-p groups should be linked to an evolution of the non-coaxiality angle θ that is expected to take non-zero values. For the purpose of this analysis, the strain evolution of the mean absolute non coaxiality ($<|\theta|>$) is shown in Figure 23.

During the hardening phases (Stage I and II), the geometrical orientation of 3-p groups tend to align to the axial loading direction. At the stress peak ($\varepsilon_{22} = 0.014$), the mean absolute non-coaxiality reaches its minimum value $<|\theta|>= 25°$. As the major direction of stress is closer to the major loading direction than that of the geometry (Figure 21 and 22), the pilot role of the mesoscopic stress distribution in the loading direction is then identified before Stage III. After the stress peak, $<|\theta|>$ increases both inside and outside the shear band. 3-p groups rotate under the plausible combined

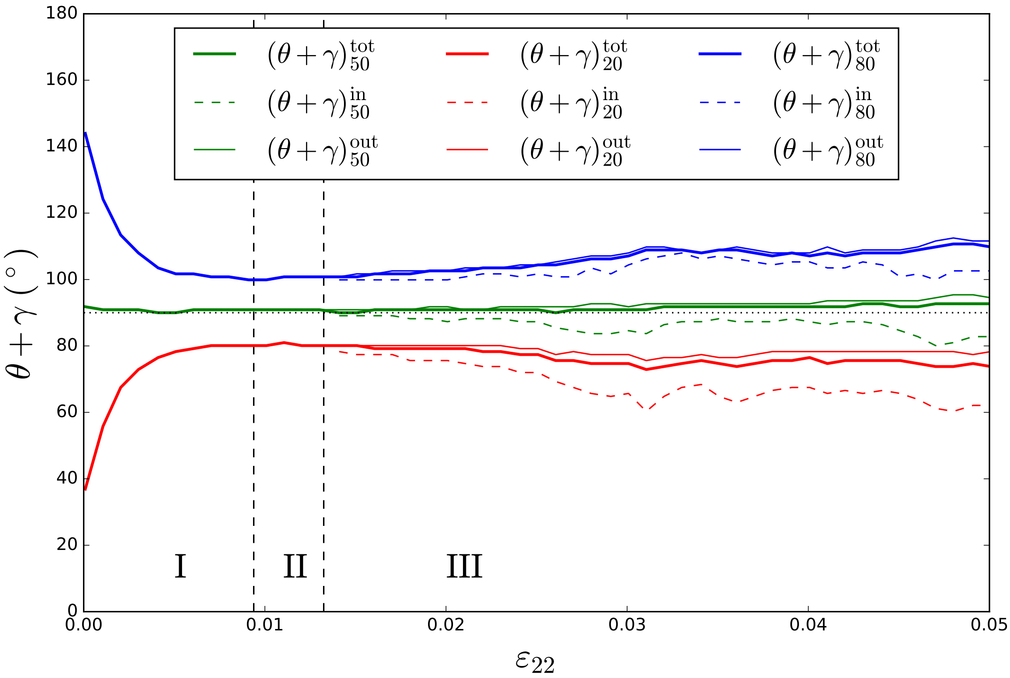

Figure 22: Strain evolution of the 20 %, 50 % and 80 % passing fractions of the cumulated distributions of the principal stress direction orientation $\gamma+\theta$ of 3-p groups. After the stress peak, cumulative distributions are computed separately inside and outside the shear band.

influence of the non coaxial stress and the release in kinematic constraints. Because the direction of the meso-stress is strongly influenced by the macroscopic boundary conditions, it does not rotate as much as the geometry and the non-coaxiality increases again. Besides, if we connect the present definition of force chain based on grain compression stresses with the other classical definition of force chains based on contact force networks (see Radjai et al. (1998) for instance), the geometrical rotation of 3-p groups is expected to change the internal stress distribution. Indeed, the meso-stress component initially aligned in vertical direction rotates and contribute to the lateral macro stress. As the macro lateral stress is imposed as constant (drained biaxial loading conditions), the meso-stress with the major direction oriented within a certain lateral sector will decrease accordingly. Therefore, large 3-p group rotations inside the shear band might be a contributor to the macro structural softening.

5. Conclusion and outlook

The structural strain softening observed in biaxial tests is revisited in this paper with mesoscopic analyses. Perspectives at the mesoscale are focused on, including geometrical and mechanical evolutions of basic force chain elements (3-p groups) and their surrounding loops. By investigating the stress, fabric, confining loops and rotations of force chains at this elementary mesoscale, new findings

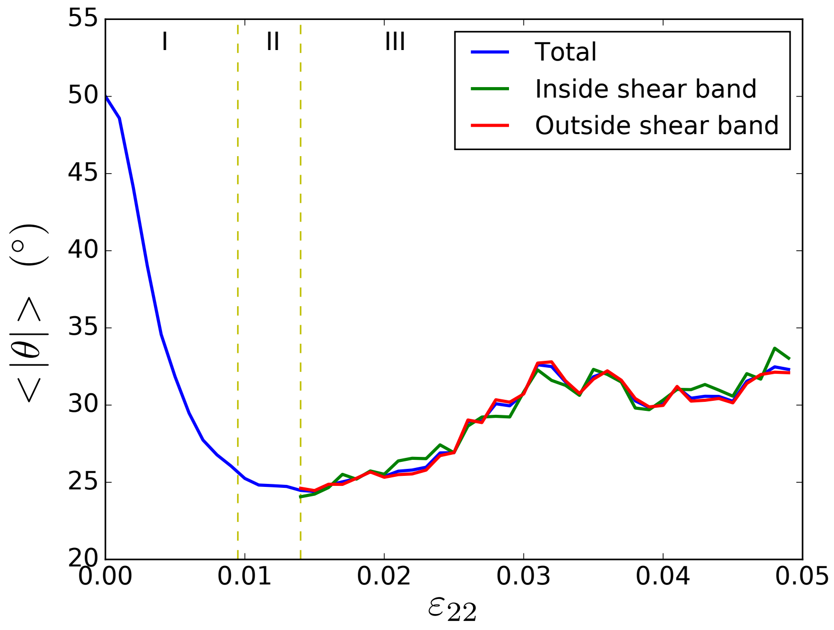

Figure 23: Evolution of the mean non coaxial angle $<|\theta|>$ during the biaxial test for the dense sample. As the shear loading develops, $<|\theta|>$ is computed separately inside and outside the shear band.

for both hardening and softening mechanisms are presented, which can be summarized as follows:

1. Dense and loose assemblies react differently as the deviatoric loads are applied. Structural softening is identified for the dense specimen, with a final shear band forming. Using the meso-stress definition based on 3-p groups, it has been shown that the meso softening also exists locally in the solid phase of the granular sample. Also, the macroscopic softening is not simply due to the geometric stress reduction coming from the increase in porosity.

2. The stress-strain relations for the dense assembly can be divided into three phases: hardening with contractancy (Stage I), hardening with dilatancy (Stage II) and softening with dilatancy (Stage III). At the mesoscale, the force chain population, relative stress, fabric and associated topology exchanges are explored for all the three stages. For the first stage of hardening (Stage I), the number of chained particles increases, force chains straighten and surrounding voids shrink. This contributes to the robustness of the granular assembly and the persistence of the force network, allowing for reversibility to a certain extent (quasi-elastic domain). For Stage II, as dilatancy occurs, no new force chains are built and stress concentrates within existing force chains. As contacts are continuously lost, force chains have more and more kinematic degrees of freedom to evolve. At this stage, the persistence of the force network is more and more compromised.

3. During Stage III, the meso-stress is highly concentrated on force chains, the recti-linearity of which decreases (mesoscopic fabric anisotropy). As a shear band develops, the two homogeneous domains inside and outside the shear band are analyzed separately. Mesoscopic geometry and stress rotations within the shear band are shown to differ from those outside the shear band at the scale of 3-p groups. Finally, the non-coaxiality between geometry and stress contributes to the mesoscopic softening.

4. At the level of 3-p groups, a meso-stress definition is proposed with and without taking into account the surrounding voids. The corresponding statistics of meso-stresses give qualitative correspondence to the macro stress, and with respect to the meso-stress of 3-p groups, the heterogeneity of force transmission is also identified. The force chain rotation of the 3-p group provides a sound micromechanical explanation for the observed macroscopic strain softening. 3-p group rotation contributes to transfer the vertical load on the lateral boundaries. As the lateral stress is imposed as constant, the vertical stress adapts accordingly, leading to the macroscopic softening. This result connects material scale properties to the boundary conditions and relates thus to structural softening. It has been derived here for a particular sample of aspect ratio 1.5 but a parametric study has shown that it can be generalized for other aspect ratios. The aspect ratio influences however the shear band direction which will be discussed in a forthcoming paper.

This study has shown once again the relevance of mesoscale structures to capture the physics of granular materials. A number of statistical observations provide mesoscale clues to understand the meso origin of hardening and softening in granular materials. 3-p group rotation has been shown to contribute to this softening but this does not exclude other mesoscale mechanisms. By accounting for spatial correlations between the introduced mesostructures, we envision to extend our mesoscale description of granular materials in order to precise the mesoscale definition of buckling or softening which has been shown to be irrelevant at the scale of 3-p groups.

The mesoscale analysis presented in this paper can also be used to bridge the gap between discrete and continuum descriptions of granular materials at a scale where the concept of representative elementary volume (REV) does not hold (the scale separation hypothesis required to define a REV is not fulfilled at mesoscale). This will pave the way for a micromechanical analysis of slip lines and shear bands as defined within continuum mechanics framework (discontinuities in the displacement and strain fields respectively).

Acknowledgements

This work was supported by National Key R&D Program of China (No. 2018YFC1508500), China Scholarship Council (Joint PhD program, No. 201606270088) and China Postdoctoral Science Foundation (No. 2018M642910)

We gratefully acknowledge the CNRS International Research Network GeoMech for having offered the opportunity to kick start this project through the organization of many workshops with topics connected to the concepts developed in this paper (http://gdr-mege.univ-lr.fr/).

We thank all the anonymous reviewers for their helpful suggestions on the quality improvement of our paper.

References

Bagi, K., 1996. Stress and strain in granular assemblies. Mechanics of materials 22 (3), 165–177.

Been, K., Jefferies, M. G., 1985. A state parameter for sands. Géotechnique 35 (2), 99–112.

Bonelli, S., Millet, O., Nicot, F., Rahmoun, J., De Saxcé, G., 2012. On the definition of an average strain tensor for two-dimensional granular material assemblies. International Journal of Solids and Structures 49 (7-8), 947–958.

Cambou, B., Jean, M., Radjai, F., 2013. Micromechanics of granular materials. John Wiley & Sons.

Dafalias, Y. F., Jun 2016. Must critical state theory be revisited to include fabric effects? Acta Geotechnica 11 (3), 479–491.
URL https://doi.org/10.1007/s11440-016-0441-0

Dedecker, F., Chaze, M., Dubujet, P., Cambou, B., 2000. Specific features of strain in granular materials. Mechanics of Cohesive-frictional Materials 5 (3), 173–193.

Frenning, G., Alderborn, G., 2005. Evolution of distributions and spatial correlations of single-particle forces and stresses during compression of ductile granular materials. Physical Review E 71 (1), 011305.

Guo, N., Zhao, J., 2013. The signature of shear-induced anisotropy in granular media. Computers and Geotechnics 47, 1–15.

Iwashita, K., Oda, M., 2000. Micro-deformation mechanism of shear banding process based on modified distinct element method. Powder Technology 109 (1-3), 192–205.

Kawamoto, R., Andò, E., Viggiani, G., Andrade, J. E., 2018. All you need is shape: Predicting shear banding in sand with ls-dem. Journal of the Mechanics and Physics of Solids 111, 375–392.

Kruyt, N., Rothenburg, L., 1996. Micromechanical definition of the strain tensor for granular materials. Appi. Mech 118, 706–711.

Kruyt, N. P., 2010. Micromechanical study of plasticity of granular materials. Comptes rendus mécanique 338 (10-11), 596–603.

Kruyt, N. P., Millet, O., Nicot, F., 2014. Macroscopic strains in granular materials accounting for grain rotations. Granular matter 16 (6), 933–944.

Kruyt, N. P., Rothenburg, L., 2016. A micromechanical study of dilatancy of granular materials. Journal of the Mechanics and Physics of Solids 95, 411–427.

Kuhn, M. R., 1999. Structured deformation in granular materials. Mechanics of materials 31 (6), 407–429.

Lade, P. V., 1977. Elasto-plastic stress-strain theory for cohesionless soil with curved yield surfaces. International Journal of Solids and Structures 13 (11), 1019–1035.

Li, X., Dafalias, Y. F., 2000. Dilatancy for cohesionless soils. Géotechnique 50 (4), 449–460.

Li, X., Yu, H.-S., 2009. Influence of loading direction on the behavior of anisotropic granular materials. International Journal of Engineering Science 47 (11), 1284–1296.

Li, X., Yu, H.-S., 2013. On the stress–force–fabric relationship for granular materials. International Journal of Solids and Structures 50 (9), 1285–1302.

Li, X. S., Dafalias, Y. F., 2012. Anisotropic critical state theory: Role of fabric. Journal of Engineering Mechanics 138 (3), 263–275.

Liu, J., Nicot, F., Zhou, W., 2018. Sustainability of internal structures during shear band forming in 2d granular materials, accepted.

Love, A., 1927. A treatise on the mathematical theory of elasticity, cambridge university press. Cambridge.

Ma, G., Regueiro, R. A., Zhou, W., Liu, J., 2018. Spatiotemporal analysis of strain localization in dense granular materials. Acta Geotechnica, 1–18.

Ma, G., Zhou, W., Chang, X.-L., 2014. Modeling the particle breakage of rockfill materials with the cohesive crack model. Computers and Geotechnics 61, 132–143.

Ma, G., Zhou, W., Regueiro, R. A., Wang, Q., Chang, X., 2017. Modeling the fragmentation of rock grains using computed tomography and combined fdem. Powder Technology 308, 388–397.

Maeda, K., Kuwabara, N., Matsuoka, H., 2001. Micromechanical analysis on formation process of microstructure in granular material during compression and shear. Kishino, éditeur: Powders and Grains, 223–226.

Nguyen, N.-S., Magoariec, H., Cambou, B., 2012. Local stress analysis in granular materials at a mesoscale. International Journal for Numerical and Analytical Methods in Geomechanics 36 (14), 1609–1635.

Nicot, F., Darve, F., 2011. The h-microdirectional model: accounting for a mesoscopic scale. Mechanics of Materials 43 (12), 918–929.

Nicot, F., Xiong, H., Wautier, A., Lerbet, J., Darve, F., 2017. Force chain collapse as grain column buckling in granular materials. Granular Matter 19 (2), 18.

Oda, M., 1982. Fabric tensor for discontinuous geological materials. Soils and Foundations 22 (4), 96–108.

Oda, M., Kazama, H., 1998. Microstructure of shear bands and its relation to the mechanisms of dilatancy and failure of dense granular soils. Géotechnique 48 (4), 465–481.

Peters, J. F., Muthuswamy, M., Wibowo, J., Tordesillas, A., 2005. Characterization of force chains in granular material. Physical review E 72 (4), 041307.

Radjai, F., Jean, M., Moreau, J.-J., Roux, S., 1996. Force distributions in dense two-dimensional granular systems. Physical review letters 77 (2), 274.

Radjai, F., Wolf, D. E., Jean, M., Moreau, J.-J., 1998. Bimodal character of stress transmission in granular packings. Physical review letters 80 (1), 61.

Rechenmacher, A. L., Abedi, S., Chupin, O., Orlando, A. D., 2011. Characterization of mesoscale instabilities in localized granular shear using digital image correlation. Acta Geotechnica 6 (4), 205–217.

Rothenburg, L., Bathurst, R., 1989. Analytical study of induced anisotropy in idealized granular materials. Géotechnique 39 (4), 601–614.

Roux, J.-N., 2000. Geometric origin of mechanical properties of granular materials. Physical Review E 61 (6), 6802.

Satake, M., 1982. Fabric tensor in granular materials. In: Proc., IUTAM Symp. on Deformation and Failure of Granular materials, Delft, The Netherlands.

Satake, M., 1992. A discrete-mechanical approach to granular materials. International journal of engineering science 30 (10), 1525–1533.

Sibille, L., Hadda, N., Nicot, F., Tordesillas, A., Darve, F., 2015. Granular plasticity, a contribution from discrete mechanics. Journal of the Mechanics and Physics of Solids 75, 119–139.

Sterpi, D., 1999. An analysis of geotechnical problems involving strain softening effects. International Journal for Numerical and Analytical Methods in Geomechanics 23 (13), 1427–1454.

Suiker, A., De Borst, R., Chang, C., 2001. Micro-mechanical modelling of granular material. part 1: Derivation of a second-gradient micro-polar constitutive theory. Acta Mechanica 149 (1-4), 161–180.

Sun, Y., Gao, Y., Zhu, Q., 2017. Fractional order plasticity modelling of state-dependent behaviour of granular soils without using plastic potential. International Journal of Plasticity.

Tordesillas, A., 2007. Force chain buckling, unjamming transitions and shear banding in dense granular assemblies. Philosophical Magazine 87 (32), 4987–5016.

Tordesillas, A., Muthuswamy, M., 2009. On the modeling of confined buckling of force chains. Journal of the Mechanics and Physics of Solids 57 (4), 706–727.

Tordesillas, A., Pucilowski, S., Lin, Q., Peters, J. F., Behringer, R. P., 2016. Granular vortices: identification, characterization and conditions for the localization of deformation. Journal of the Mechanics and Physics of Solids 90, 215–241.

Tordesillas, A., Pucilowski, S., Walker, D. M., Peters, J. F., Walizer, L. E., 2014. Micromechanics of vortices in granular media: connection to shear bands and implications for continuum modelling of failure in geomaterials. International Journal for Numerical and Analytical Methods in Geomechanics 38 (12), 1247–1275.

Tordesillas, A., Walker, D. M., Lin, Q., 2010. Force cycles and force chains. Physical Review E 81 (1), 011302.

Šmilauer, V., et al., 2015. Yade Documentation 2nd ed. The Yade Project, http://yade-dem.org/doc/.

Walker, D. M., Tordesillas, A., 2010. Topological evolution in dense granular materials: a complex networks perspective. International Journal of Solids and Structures 47 (5), 624–639.

Wan, R., Guo, P., 1998. A simple constitutive model for granular soils: modified stress-dilatancy approach. Computers and Geotechnics 22 (2), 109–133.

Wang, J., Gutierrez, M. S., Dove, J. E., 2007. Numerical studies of shear banding in interface shear tests using a new strain calculation method. International Journal for Numerical and Analytical Methods in Geomechanics 31 (12), 1349–1366.

Wautier, A., Bonelli, S., Nicot, F., 2017. Scale separation between grain detachment and grain transport in granular media subjected to an internal flow. Granular Matter 19 (2), 22.

Wautier, A., Bonelli, S., Nicot, F., 2018. Micro-inertia origin of instabilities in granular materials. Int J Numer Anal Methods Geomech, 19.

Weber, J., 1966. Recherches concernant les contraintes intergranulaires dans les milieux pulvérulents. Bulletin de Liaison des Ponts-et-chaussées 20, 1–20.

Xiong, H., Nicot, F., Yin, Z., 2017. A three-dimensional micromechanically based model. International Journal for Numerical and Analytical Methods in Geomechanics.

Yin, Z.-Y., Hicher, P.-Y., Dano, C., Jin, Y.-F., 2016. Modeling mechanical behavior of very coarse granular materials. Journal of Engineering Mechanics 143 (1), C4016006.

Zhang, L., Nguyen, N. G. H., Lambert, S., Nicot, F., Prunier, F., Djeran-Maigre, I., 2017. The role of force chains in granular materials: from statics to dynamics. European Journal of Environmental and Civil Engineering 21 (7-8), 874–895.

Zhou, W., Yang, L., Ma, G., Chang, X., Cheng, Y., Li, D., 2015. Macro–micro responses of crushable granular materials in simulated true triaxial tests. Granular Matter 17 (4), 497–509.

Zhu, H., Nguyen, H. N., Nicot, F., Darve, F., 2016a. On a common critical state in localized and diffuse failure modes. Journal of the Mechanics and Physics of Solids 95, 112–131.

Zhu, H., Nicot, F., Darve, F., 2016b. Meso-structure organization in two-dimensional granular materials along biaxial loading path. International Journal of Solids and Structures 96, 25–37.